An efficient tree-topological local mesh refinement on Cartesian grids for multiple moving objects in incompressible flow

Wei Zhang [a], Yu Pan [a], Junshi Wang [a,1], Valentina Di Santo [b], George V. Lauder [c], Haibo Dong [a,*]

[a] *Department of Mechanical and Aerospace Engineering, University of Virginia, 122 Engineer's Way, Charlottesville, 22904, VA, USA*
[b] *Division of Functional Morphology, Department of Zoology, Stockholm University, Svante Arrhenius väg 18B, Stockholm, SE-11419, Sweden*
[c] *Department of Organismic and Evolutionary Biology, Harvard University, 26 Oxford Street, Cambridge, 02138, MA, USA*

A B S T R A C T

This paper develops a tree-topological local mesh refinement (TLMR) method on Cartesian grids for the simulation of bio-inspired flow with multiple moving objects. The TLMR nests refinement mesh blocks of structured grids to the target regions and arrange the blocks in a tree topology. The method solves the time-dependent incompressible flow using a fractional-step method and discretizes the Navier-Stokes equation using a finite-difference formulation with an immersed boundary method to resolve the complex boundaries. When iteratively solving the discretized equations across the coarse and fine TLMR blocks, for better accuracy and faster convergence, the momentum equation is solved on all blocks simultaneously, while the Poisson equation is solved recursively from the coarsest block to the finest ones. When the refined blocks of the same block are connected, the parallel Schwarz method is used to iteratively solve both the momentum and Poisson equations. Convergence studies show that the algorithm is second-order accurate in space for both velocity and pressure, and the developed mesh refinement technique is benchmarked and demonstrated by several canonical flow problems. The TLMR enables a fast solution to an incompressible flow problem with complex boundaries or multiple moving objects. Various bio-inspired flows of multiple moving objects show that the solver can save over 80% computational time, proportional to the grid reduction when refinement is applied.

© 2023 Elsevier Inc. All rights reserved.

1. Introduction

Bio-inspired flow dynamics studies the external flows perturbed by moving insects, birds, and fishes, or internal flows within the functioning organs of human and animals. It has a broad range of applications in biomimetic engineering and human health studies [1–4]. Different from canonical flow simulation problems, bio-inspired flow features unsteady flow restrained by complex boundaries, such as flexible or moving surfaces. Despite the successes of moving unstructured meshes used in a finite volume or a finite element method [5–7], Cartesian grids with immersed boundary (IB) methods [8–10] are

one of the most popular approaches for studying cases with complex boundaries. The IB method solves the Navier-Stokes equations on a fixed Cartesian grid and models the solid boundaries by a field of forces to enforce the boundary conditions and therefore enables an effective solution for moving boundary problems. The success of the IB method has attracted a great deal of research interest [11–16]. The sharp-interface immersed boundary method using a direct forcing approach achieved great success in various bio-inspired flows with complex and moving boundaries [17–20]. Despite its enormous success, the IB method poses challenges to computing resources because of the large number of mesh cells required for a smooth representation of complex boundaries. This issue can be even more demanding in flow with multiple moving objects (MMO), such as a flock of flying birds or schooling fish, which is often characterized by a large computational domain with very different grid resolution close to and far away from the solid boundaries. Hence, the design of a fast and efficient technique for such problems is an urgent need.

The local mesh refinement (LMR), or the local adaptive mesh refinement (AMR) techniques [21,22], which locally refine the mesh without significantly increasing the total number of mesh cells, mitigates the demands for computing resources and provides an attractive solution. The subdivision and the addition of new grid elements usually change the data structure. Hence, the unstructured meshes [23,24] are often recursively refined to solve the flow problem with the finite element or finite volume methods. To refine the structured grids, more advantaged data structures, such as the tree-based multi-layer grids, specifically the quadtree for two-dimensional (2D) grids [25,26] or the octree for three-dimensional (3D) grids [27–29], are commonly used to refine the cells to provide sufficient grid resolution. However, the IB method prefers simple structured Cartesian grids, like the multi-layer block-structured grids used by Berger et al. [30] for hyperbolic systems. In their approach, a sequence of blocks containing finer Cartesian grids will be automatically generated or removed by evaluating a user-specified error function until the solution is sufficiently resolved. This technique achieved substantial success on various 2D and 3D hyperbolic systems or compressible flows [31–34]. Several popular open source libraries in this line are PARAMESH [35], AMReX [36], Chombo [37] and SAMRAI [38]. A comprehensive but not necessarily complete list of the structured AMR libraries can be found in the survey of Dubey et al. [39].

The block-based AMR techniques have also been integrated with IB methods to solve the incompressible flow problem and some popular patch-based or octree-based (for 3D problem) refinement techniques have emerged [40–44]. Some of the popular open source codes of this kind include the IBAMR [45,46], implementing the IB method in an adaptive and parallel platform. Unlike compressible flow problems, which can be numerically advanced in time, incompressible flows need to solve the elliptic Poisson equation for a divergence-free velocity field. One concern is computational efficiency, such as computational time or memory, of the Poisson equation under such mesh refinement techniques, especially when the refinement contains too many small refinement blocks and hence parallel computation on a distributed memory is required. For instance, the tree-based refinement mesh, on which a hierarchy of multilevel mesh is constructed such that each level of mesh discretizes the domain using square (cubic in 3D) finite cells and each level locally refines the previous level, enables the application of the multigrid method to relax the Poisson equation effectively. This technique works well for either cell-based or block-based mesh refinement [26,27,47,48]. Nevertheless, data communication between the multilevel meshes by the Poisson solver is often inefficient for distributed-memory computing. Moreover, unique features of bio-inspired systems, including the complex topology of animals, dynamic morphing of wings and fins, and the multiple moving objects in fish schooling and bird flocking, demands a more versatile mesh refinement framework that is accurate and efficient, which brings more challenges to mesh refinement strategy and the associated data parallelization and memory management [49–52]. As an example, for a two-fish system, computational domains may reach quite high grids number, up to 49 million, to satisfy these requirements of the dense grids near the bodies and high-quality grids in the far wake [52]. Local refinement of a two-fish system is tackled too, but inability for the local refinement regions to intersect limits the spacing of the fishes and the size of the refinement regions [51]. For 3D fish schooling problems with a larger number of fishes, flow simulations require both fine mesh around the swimming fish to resolve the complex geometry and high-quality mesh in the mid- and far-field to resolve the hydrodynamic interaction between fish and the signature of the vortex wake. Therefore, a suitable refinement strategy is needed to satisfy both requirements at the lowest cost of mesh. And, because multiple mesh blocks are commonly used, parallelization scheme and memory management of mesh blocks for distributed memory systems needs to be customized and optimized together for this type of application. Peng et al. [53] demonstrated that with a few nested blocks containing Cartesian grids they can improve the discretization accuracy around the solid boundaries. Their approach is based on the finite volume approach and was applied only to 2D flow problems with stationary boundaries. Deng and Dong [54] presented an octree-like local mesh refinement technique for bio-inspired flow simulation with enhanced computation ability due to a reduced number of mesh cells. Recently, Zhang et al. [55] developed a block-based mesh refinement technique using a finite-difference formulation with IB method to simulate human airway flow with a moving uvula. Direct application of the aforementioned nested Cartesian grids to 3D flows with MMO is difficult and the computation of the Poisson equations on multiple refinement blocks needs to be carried out more efficiently on a distributed-memory system.

This paper develops a tree-topological local mesh refinement (TLMR) with IB method embedded (TLMR-IBM) flow solver for bio-inspired flow with MMO. This method recursively refines local mesh without significantly increasing the number of mesh cells. This method can be applied to unsteady flow problems with MMO and has the flexibility to adapt to highly nonuniform initial background mesh. More importantly, an effective iterative procedure is developed on these TLMR blocks for a fast solution of the momentum equation and the continuity equation. With the proposed TLMR method, an existing Cartesian-grid-based flow solver can be readily adapted and parallelized. This paper is organized as follows. § 2 introduces

the proposed mesh refinement technique and an iterative procedure to solve the discretized Navier-Stokes equation is also presented for such meshes. § 3 presents some benchmark examples and demonstrates the accuracy and efficiency of the proposed mesh refinement technique. Analyses of other complicated flows past MMO are also demonstrated to illustrate the application of this approach.

2. Numerical methods

This section introduces the mesh for TLMR and the method to integrate the incompressible Navier-Stokes equations on such mesh.

2.1. The meshes for TLMR

An MMO-friendly mesh refinement technique should let users determine where to add refined mesh blocks freely, such as regions containing immersed boundaries, strong flow-structure interactions, and/or body-body-flow interactions. As computational efficiency is of the primary concern, the current method uses a small number of big rectangular blocks that consist of a relatively large number of mesh cells rather than many small blocks. Using big blocks reduces the total number of blocks to add, which reduces inter-block communications and can be more friendly to the user. Fig. 1(a) illustrates an example of a school of fish from which the flow simulation can benefit from the TLMR method. To simulate flow around such a group, dense mesh are required around each swimmer. Instead of having a uniform mesh for the computational domain, we can gradually refine the mesh with refined blocks. For the problem illustrated in Fig. 1(a), one block with the background Cartesian grids covers the whole computational domain. Then another block covers the school with an additional refinement block around each fish for better resolution. To better resolve the body-body/fin interaction between different sizes of fishes, one more refinement block can be placed around the smaller fish. If the wake is of interest, an additional refinement block is placed in the far wake region.

The above refinement technique nests the fine blocks inside the coarse ones to achieve fine grid resolution in the given region. The parent and child hierarchy of refinement blocks resembles a tree topology, which is employed to describe the connectivity between the blocks and the communications between them. As referenced in Fig. 1(b), each block is a node of the tree and its refinement block is its child node. The refinement level of the block is defined as the number of blocks back to the root node. Hence, block 0 is on level 0, and block 1 and block 2 are on level 1, as shown in Fig. 1(b). We further restrict that each node can have only one parent block, meaning that a refinement block must be located inside one coarse block. This restriction degrades slightly the flexibility of adding refinement blocks but the simplified connectivity greatly reduces the communication complexity between the refinement blocks.

In addition to the apparent parent-child connection, the child blocks sharing the same parent block can also be connected, such as block 1 (B1)-B2 or B3-B4, labeled by the dashed lines in Fig. 1(b). The two types of connectivity not only differ from the viewpoint of the topology but also significantly impact the efficiency of solving equations discretized on the TLMR blocks. Therefore, the two types of connections are distinguished in the current TLMR method using the terms interlayer-connection and intralayer-connection, where the former describes the relation of a fine block lying inside a coarse block and the latter denotes the overlapping of child blocks within the same parent block.

Mesh cells in the refined block are obtained by subdividing that of the coarse block in each direction by a factor of two. Hence, a 3D cell will have eight subcells or four for a 2D case. By adjusting the resolution of background mesh and the total levels of refinements, the local refinement approach can provide the desired grid resolution around interested regions without significantly increasing the overall number of mesh cells. The boundary-induced mesh refinement of bio-inspired flows often adopts a fixed hierarchical mesh refinement and does not need to be changed during the simulation. These predetermined mesh blocks can avoid the overhead of dynamic allocation and deallocation of grids in a standard AMR technique.

2.2. Fractional-step method for incompressible Navier-Stokes equations with immersed boundaries

The bio-inspired flow is usually described by the unsteady incompressible Navier-Stokes equations

$$\frac{\partial u_i}{\partial t} + \frac{\partial \left(u_i u_j \right)}{\partial x_j} = -\frac{\partial p}{\partial x_i} + \frac{1}{Re}\frac{\partial^2 u_i}{\partial x_j x_j}, \tag{1}$$

$$\frac{\partial u_i}{\partial x_i} = 0, \tag{2}$$

where $i, j = 1, 2,$ or 3, and $u_1, u_2,$ and u_3 are the dimensionless velocity in x-, y-, and z-direction respectively, and p is the dimensionless pressure of the fluid. Re is the Reynolds number.

The incompressible Navier-Stokes equations are discretized using a cell-centered, collocated arrangement of the primary variables u_1, u_2, u_3, and p. The coupled system of velocity and pressure is integrated in time using the fractional-step method [56,57], where it first computes an approximation solution $\boldsymbol{u}^*$ to the momentum Eqn. (1) by
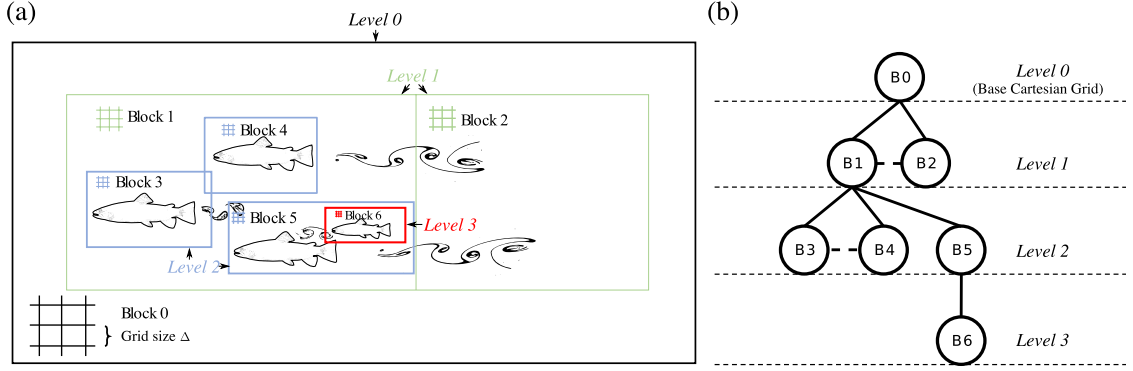
Fig. 1. Schematic of TLMR for flow with multiple moving objects: (a) a bio-inspired flow problem with local mesh refinement and (b) a tree topology for the refinement blocks, with solid lines denoting interlayer connections and dash lines for intra-layer connections.

$$\frac{u_i^* - u_i^n}{\Delta t} = \frac{1}{2}\left(3N_i^n - N_i^{n-1}\right) + \frac{1}{2Re}\left(\frac{\delta^2}{\delta x^2} + \frac{\delta^2}{\delta y^2} + \frac{\delta^2}{\delta z^2}\right)\left(u_i^n + u_i^*\right), \tag{3}$$

using a second-order Adams-Bashforth scheme for the convective terms and an implicit Crank-Nicolson scheme for the viscous term to eliminate the viscous stability constraint. Nonlinear convective terms are represented as $N_i = -\delta(u_i u_j)/\delta x_j$. $\delta/\delta x_j$ represents a second-order central difference for the first derivative. The divergence-free restriction is applied through the projection

$$\frac{u_i^{n+1} - u_i^*}{\Delta t} = -\frac{\delta\phi^{n+1}}{\delta x_i}, \tag{4}$$

where ϕ follows the Poisson equation

$$\left(\frac{\delta^2}{\delta x^2} + \frac{\delta^2}{\delta y^2} + \frac{\delta^2}{\delta z^2}\right)\phi^{n+1} = \frac{1}{\Delta t}\frac{\delta u_i^*}{\delta x_i}, \tag{5}$$

where $\delta^2/\delta x_i^2$ represents the second-order central difference of the Laplacian operator in the x, y, and z-direction and $\delta\phi^{n+1}/\delta x_i$ is the Einstein notation for $\delta u_1^*/\delta x + \delta u_2^*/\delta y + \delta u_3^*/\delta z$. The pressure can be recovered from $p^n = \phi^n$ with a truncation error of $O(\Delta t/Re)$ [56].

To resolve the immersed boundary, the sharp-interface IB method developed by Mittal et al. [19] is adopted and the implementation has been tested extensively in the previous works [58–60].

2.3. An efficient iterative solver on the TLMR mesh

2.3.1. A parallel computation design on the TLMR mesh

Though the present TLMR method does not require parallel computation, it is nevertheless most efficient to do so. The primary reason is that the number of mesh cells within each block is often large, especially for 3D applications, and therefore a distributed-memory storage is essential. Secondly, the storage arrangement is beneficial for the development of the TLMR-based flow solver. A LMR flow solver can be readily adapted from an established Cartesian grid flow solver because the structured Cartesian grids as well as the data structures are preserved on these computing nodes.

The storage arrangement is advantageous for the hybrid parallelism. Firstly, blocks with a large mesh cell number can be computed individually and their information can be exchanged only at the interface using the message passing interface (MPI), yielding the coarse-grained parallel computation. Secondly, fine-grained parallel computation is achieved by multi-threading the computation of each block with the Cartesian grids. The threading enables extra freedom to control load balance among a distributed memory system by setting the thread number for each block so the number of mesh cells per thread is approximately equal for all blocks. Hence, the present TLMR method can benefit from the hybrid parallelism performed on computer systems connected by multiple nodes with multi-core processors.

Although the aforementioned discretized equations can be solved iteratively using an iterative algorithm on each TLMR block whose mesh is divided into logically disjoint chunks without overlap, the iterative convergence can be significantly affected by this approach. Furthermore, several differences exist when solving the momentum and the elliptic Poisson equations considering the dramatically different iterative convergence properties of the two types of equations. The following sections describe several techniques to improved the iterative convergence. The discussions in section 2.3 are primarily for solving the momentum equation on the TLMR mesh. Although the procedures described here apply to solving the Poisson equation, a fast iterative Poisson solver on the TLMR mesh is introduced in section 2.4.

(a)   (b)

5-point stencil for regular cell
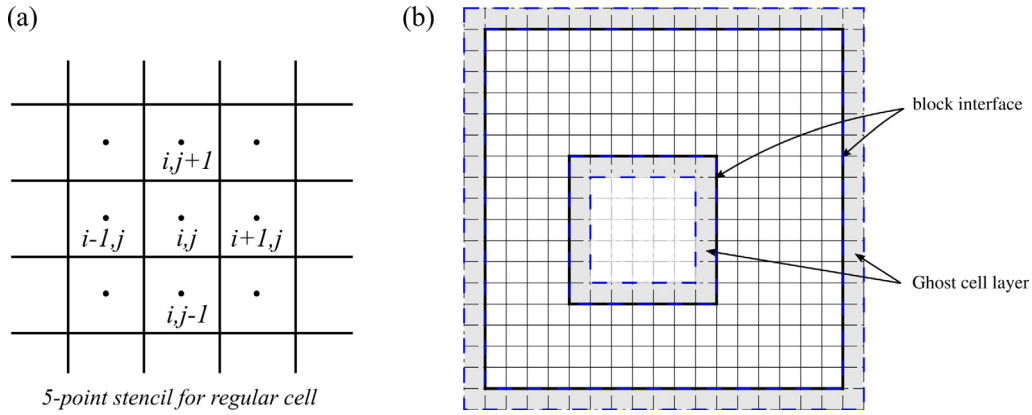
Fig. 2. Illustration of discretization stencil and the ghost cell arrangement for a refined block: (a) a 5-point discretization stencil for a fluid cell and (b) the arrangement of ghost cell layers (shaded) around the block interfaces.

Discretization on the TLMR mesh incorporating layers of ghost cells

The discretized momentum (3) and the Poisson equation (5) on the Cartesian grids at the cell (i, j, k) can be reformulated to the following form

$$
\begin{aligned}
a_{i-1,j,k}\psi_{i-1,j,k} + a_{i,j-1,k}\psi_{i,j-1,k} &+ a_{i,j,k-1}\psi_{i,j,k-1} + a_{i,j,k}\psi_{i,j,k} \\
&+ a_{i+1,j,k}\psi_{i+1,j,k} + a_{i,j+1,k}\psi_{i,j+1,k} + a_{i,j,k+1}\psi_{i,j,k+1} \quad = RHS_{i,j,k},
\end{aligned}
\tag{6}
$$

where $\psi_{(\cdot)}$ is the discretized value for velocity (u, v and w) or pressure (p) and $a_{(\cdot)}$ is the corresponding coefficient in the discretized equations. The discretization leads to a 7-point stencil for a 3D application, or a 5-point stencil for a 2D application as conveniently illustrated in Fig. 2(a).

As data of different blocks are stored in a distributed fashion, the discretization scheme requires a ghost cell when performed at the boundary of each block. For parallel computation, a layer of ghost cells is arranged at the block interface, as illustrated in Fig. 2(b). A block will have an outer ghost cell layer if it resides in a coarse block and multiple inner ghost cell layers if it contains refined blocks. With the arrangement of ghost layers, the refined block will logically cut a hole out of the coarse block. Therefore, the mesh is divided into logically disjointed parts where the momentum equation is iteratively solved. The mesh cells in the refined region in the TLMR blocks do not hold valid values for velocity $\boldsymbol{u}$ and its approximate solution $\boldsymbol{u}^*$. Therefore, when solving the momentum equation, the mesh cells of the coarse and fine blocks are not overlapped, and the values of these mesh cells need to be updated simultaneously.

### 2.3.2. An iterative solver and block-communicating strategies on the TLMR mesh

The discretized equation (6) can be solved using an iterative algorithm so a convergent solution can be achieved on all blocks. Some iterative methods such as Jacobi or successive over-relaxation (SOR) can be adopted, or one can use the popular Krylov subspace methods such as generalized minimal residual method (GMRES) [61] and the biconjugate gradient stabilized method (BiCGSTAB) [62]. In this study, an incomplete LU factorization method, modified strongly implicit procedure (MSIP) [63–65], is adopted for its simple implementation and fast convergence. To further improve the computation speed on a multi-core computer system, the MSIP algorithm is threaded.

To proceed with the iterative procedures on the block refinement mesh, ghost cell values need to be synchronized among the distributed memories. To communicate between blocks, the two types of block connections, as shown in the tree topology in Fig. 1(b), need to be considered. The first is the inter-layer connection of two blocks between two different refinement levels, and the second is the intra-layer connection of two blocks in the same refinement level.

The inter-layer communication with multidimensional Lagrange interpolation

Inter-layer communication synchronizes ghost cell values between the coarse and fine blocks. Locally defined polynomials are used to interpolate the data stored at cell centers on the current level onto cell centers at the desired level. To preserve the spatial order of accuracy of the method, second-order polynomials are used when interpolating from a coarse block to a fine block, and third-order polynomials are used in moving from fine to coarse. Denoting this polynomial order as n, the interpolation is constructed using the $n + 1$ nearest stored data points from the level with the stored data to the cell center at the desired level. Denoting these set of indices in the x, y, and z directions respectively as $[L_1, ..., L_2]$, $[M_1, ..., M_2]$, $[N_1, ..., N_2]$, the local polynomial representation of one of the state variables is given by

$$
\psi(x, y, z) = \sum_{k=N_1}^{N_2} \sum_{j=M_1}^{M_2} \sum_{i=L_1}^{L_2} \psi_{ijk} r_i(x) s_j(y) t_k(z),
\tag{7}
$$
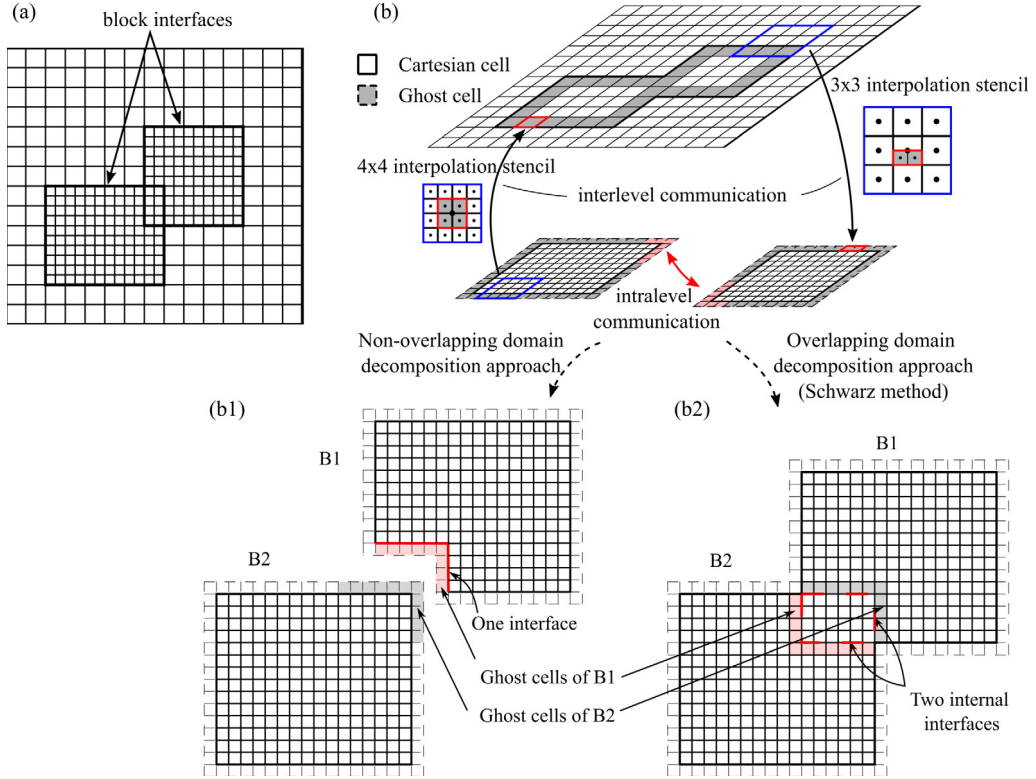
Fig. 3. Schematic of information synchronization between refinement blocks: (a) a three-block mesh refinement example, (b) the inter-layer and intra-layer communication for ghost cells (shaded) at the block interface. For the 2D example, the inter-layer communication requires interpolating from coarse to fine cells (or vice versa), through the surrounding cells using a 3×3 (or 4×4) stencil, marked by the blue squares, to the target cells, marked by the red squares (color online), and (b1, b2) two strategies to synchronize the ghost cell values among two intra-connected blocks: (b1) synchronization across one interface and (b2) simultaneous synchronization at the two interfaces. (For interpretation of the colors in the figure(s), the reader is referred to the web version of this article.)

where $\psi(x, y, z)$ is the value to be interpolated at coordinate (x, y, z) and ψ_{ijk} are the values of ψ at the Cartesian cells $\{[x_{L_1}, \cdots, x_{L_2}] \times [y_{M_1}, \cdots, y_{M_2}] \times [z_{N_1}, \cdots, z_{N_2}]\}$. The one-dimensional Lagrange polynomials $r_i(x)$, $s_j(y)$, $t_k(z)$ are defined at the x, y, and z directions respectively as

$$r_i(x) = \prod_{i' \neq i,\, L_1 \leq i' \leq L_2} \frac{x - x_{i'}}{x_i - x_{i'}}, \quad s_j(y) = \prod_{j' \neq j,\, M_1 \leq j' \leq M_2} \frac{y - y_{j'}}{y_j - y_{j'}}, \quad t_k(z) = \prod_{k' \neq k,\, N_1 \leq k' \leq N_2} \frac{z - z_{i'}}{z_k - z_{k'}},$$

with $i \in [L_1, L_2]$, $j \in [M_1, M_2]$ and $k \in [N_1, N_2]$. Fig. 3 illustrates the synchronization of ghost cell values on a 2D mesh, which contains both inter- and intra-layer connections, as shown in Fig. 3(a). A 3×3 interpolation stencil, marked by the blue square in Fig. 3(b), is used to interpolate the coarse cell values to the ghost cell in the fine block. Meanwhile, a 4×4 stencil is used to interpolate from the fine to the coarse. Likewise, for a 3D simulation, the interpolation stencils are $3 \times 3 \times 3$ and $4 \times 4 \times 4$ respectively. This interpolation strategy guarantees at least second-order accuracy in space and is crucial for the spatial accuracy of the mesh refinement technique.

The intra-layer communication using the Schwarz method for fast convergence

The intralayer-connected blocks is another factor that perplexes the communication on the TLMR blocks and has a great impact on the performance of an iterative solver. As an intralayer-connected block has finer cells and more accurate values than the coarse parent block and no interpolation is needed, it is more reasonable to synchronize the ghost-cell value from this fine block rather than the coarser parental block. In general, two strategies can be adopted in this scenario.

The first and straightforward strategy to communicate the ghost cell values results from the standard domain decomposition approach that divides the mesh cells of the two overlapped blocks into two logically disjoint chunks, as illustrated in Fig. 3(b1). The two chunks of mesh cells have only one interface between them, and then the information is exchanged through the ghost cells across the interface.

Another domain decomposition approach comes from Schwarz [66], who suggested that the two overlapped blocks were updated alternatively with updated boundary values from the other block. He explored the alternative updating strategy and proved it to be convergent. The benefits of Schwarz's method for parallel computing have been realized by several
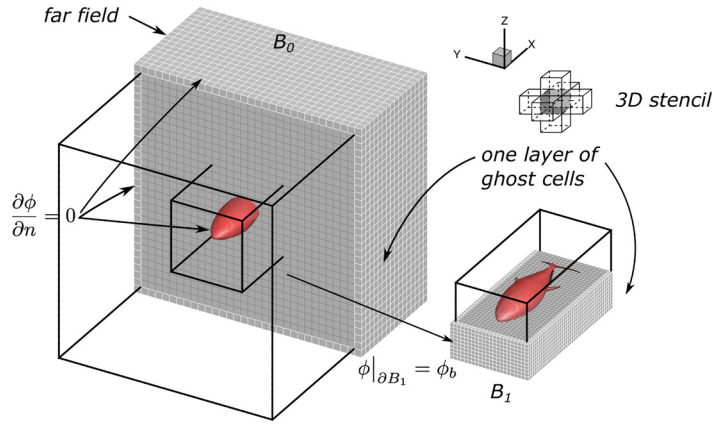
Fig. 4. Schematic of solving the Poisson equation recursively from a coarse block to a fine block, of which the boundary values on the ghost cells are interpolated from the coarse block.

researchers [67–69], who recommended simultaneously updating the boundary values of the overlapped blocks from each other during the iteration. The corresponding formulas are as follows

$$
\begin{aligned}
\psi_{\partial B_1, ijk}^{n+1} &= \psi_{B_2, i'j'k'}^{n}, \\
\psi_{\partial B_2, ijk}^{n+1} &= \psi_{B_1, i'j'k'}^{n},
\end{aligned}
\tag{8}
$$

where B_1 and B_2 are the two connected blocks as referenced in Fig. 3(b2), and ijk denotes the index of the boundary cells of B_1 or B_2 while $i'j'k'$ indexes the corresponding cells in the other block (B_2 or B_1 correspondingly), and n denotes the iterative step. It is apparent from equation (8) that the Schwarz method synchronizes boundary values at the two interfaces, different from the one interface used in the first strategy. Our numerical experiments also show that the Schwarz method can save $10\% \sim 30\%$ computation time when solving the momentum equation with intralayer-connected blocks. Hence, the Schwarz method is suggested instead of the first strategy.

2.4. Efficient Poisson solver on the TLMR mesh

As mentioned earlier, the Poisson equation often converges slowly and takes a great deal of computation time when solved iteratively, such as by the iterative algorithms mentioned before. For fast convergence, a multigrid method [70,71] is often adopted when solving this equation. The main idea of multigrid to accelerate the convergence of an iterative method is to improve the fine grid solution by a global correction obtained on a coarse grid. This is particularly useful for systems like the Poisson equations that exhibit different rates of convergence for short- and long-wavelength components, as suggested by the Fourier analysis [72].

A multigrid algorithm of block refinement mesh on a shared memory system is straightforward since the multigrid algorithm can perform the prolongation and restriction operation between coarse and fine mesh effortlessly on the multi-level refinement mesh [40]. However, care is needed on the present local refinement mesh as they are stored on distributed memories and the prolongation and restriction operation invoke communicating a large volume of data between blocks [47] and reduce overall computation speed. Besides, as pointed out by Liu and Hu [43], the algebraic multigrid method performed on the multilayer mesh, constructed from either patch-based or octree-based [35,36], often lacks scalability for large-scale parallel computation. In the following sections, strategies for a fast Poisson solver on such mesh is introduced.

2.4.1. A recursive Poisson solver on the TLMR mesh

For the coarse and fine mesh, the Poisson equation is solved recursively from the coarse block to the fine ones. Then the Poisson equation is first solved on the coarsest block and then the finer blocks, where the latter proceeds as its boundary values are interpolated from the former. This solution process can be illustrated using the two-block problem in Fig. 4. The Poisson equation is first solved on block B_0 on all fluid cells with the given Neumann boundary conditions on the far field and the solid boundaries. Then block B_1 is solved with its boundary value ϕ_b, synchronized from the block B_0, and the Neumann boundary condition at the solid boundaries. For computation efficiency, the boundary value ϕ_b is synchronized at every iteration instead of waiting for the convergence of its parent block. Different from the momentum equation, the mesh of the coarse blocks does not have a hole in the refined region. This recursive Poisson solver is similar to the level-by-level solution proposed by Guillet and Teyssier [73], who have tested and verified its efficiency on an octree-based AMR approach.

Restricting the velocity divergence $\nabla \cdot \boldsymbol{u}^*$ from a fine block to a coarse block

To solve the Poisson equation on each block, either the intermediate velocity $\boldsymbol{u}^*$ or the divergence $\nabla \cdot \boldsymbol{u}^*$ needs to be synchronized to fill the refined region from the refined blocks prior solving the Poisson equation as data are stored in a
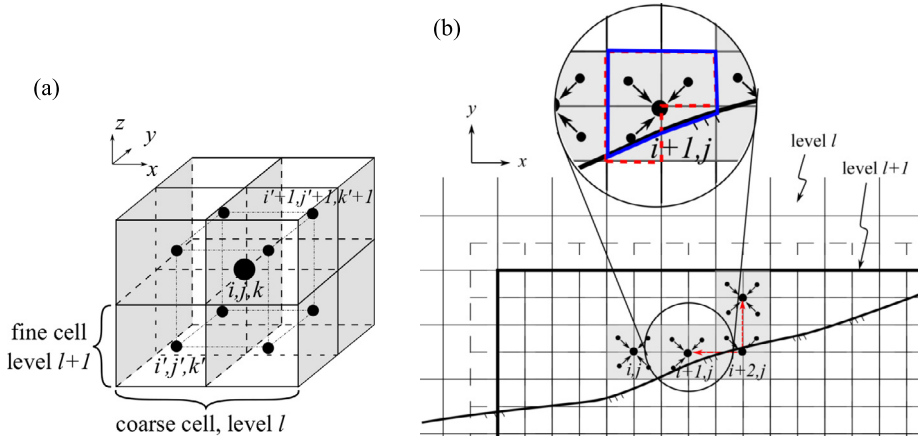
Fig. 5. Restriction of the velocity divergence $\nabla \cdot \boldsymbol{u}^*$ from fine cells to a coarse cell: (a) restriction of regular 3D cells and (b) restriction of 2D cells near a solid boundary.

distributed fashion. Considering that $\boldsymbol{u}^*$ costs three times data to communicate compared to $\nabla \cdot \boldsymbol{u}^*$, the divergence $\nabla \cdot \boldsymbol{u}^*$ is communicated in the current approach. Restricting $\nabla \cdot \boldsymbol{u}^*$ from fine cells to coarse ones on the Cartesian mesh yields

$$\left(\nabla \cdot \boldsymbol{u}^* \right)^l_{ijk} = \frac{1}{2^N} \sum_{i'j'k'} \left(\nabla \cdot \boldsymbol{u}^* \right)^{l+1}_{i'j'k'}, \tag{9}$$

where N is the dimension of the flow problem so 2^N is the total number of subcells to be averaged, and l denotes the level of refinement, with level $l+1$ mesh subdividing that of level l, as illustrated in Fig. 5(a). The index ijk denotes the coarse cell and $i'j'k'$ denotes the corresponding subcells. The divergence component $\delta u^*/\delta x$ of cell (i,j,k) at the refinement level l can be derived from the surface velocity $u^*_{i\pm 1/2,j,k}$ by

$$
\begin{aligned}
\left(\frac{\delta u^*}{\delta x} \right)^l_{ijk} &= \frac{u^*_{i+\frac{1}{2},j,k} - u^*_{i-\frac{1}{2},j,k}}{\Delta x} = \frac{\frac{1}{4}\sum_{k'=2k-1}^{2k}\sum_{j'=2j-1}^{2j} u^*_{2i+\frac{1}{2},j',k'} - \frac{1}{4}\sum_{k'=2k-1}^{2k}\sum_{j'=2j-1}^{2j} u^*_{2i-\frac{3}{2},j',k'}}{\Delta x} \\
&= \frac{1}{8}\frac{\sum_{k'=2k-1}^{2k}\sum_{j'=2j-1}^{2j}\sum_{i'=2i-1}^{2i}\left(u^*_{i'+\frac{1}{2},j',k'} - u^*_{i'-\frac{1}{2},j',k'} \right)}{\frac{1}{2}\Delta x} = \frac{1}{8}\sum_{k'=2k-1}^{2k}\sum_{j'=2j-1}^{2j}\sum_{i'=2i-1}^{2i}\left(\frac{\delta u^*}{\delta x} \right)^{l+1}_{i'j'k'},
\end{aligned}
\tag{10}
$$

where cells $(i',j',k') \in [2i-1, 2i] \times [2j-1, 2j] \times [2k-1, 2k]$ at level $l+1$ are the subcells of the cell (i,j,k). Similar relations hold for $\delta v^*/\delta y$ and $\delta w^*/\delta z$, therefore yield Eqn. (9).

When solid boundaries cut through the subcells, $\nabla \cdot \boldsymbol{u}^*$ restricts to coarse cells in a manner to preserve the cell average as indicated by Eqn. (9), with solid subcells assigned value 0. For instance, in the example in Fig. 5(b), cell $(i+1,j)$ will contain the average value of three fluid cells and one solid cell. If the coarse cell is solid, like cell $(i+2,j)$, the restricted $\nabla \cdot \boldsymbol{u}^*$ from fine subcells will be evenly redistributed to the surrounding fluid cells to keep the conservation of $\nabla \cdot \boldsymbol{u}^*$.

2.4.2. Parallel Schwarz method for intralayer-connected refinement blocks

When intralayer-connected blocks appear, our experience shows that the Schwarz method introduced in § 2.3.2 almost leverages the full power of a multigrid algorithm and converges much faster than a domain decomposition approach with no overlapping. The two-interfacial exchanging approach allows much more efficient information exchange across the overlapped refinement blocks during the multigrid sweeps. Furthermore, the Schwarz method allows computing on each rectangular block without cutting out the overlapped region, and therefore favors a multigrid algorithm on structured mesh without the need for an algebraic multigrid method, where the latter involves extra storage and can be difficult to implement.

After the design of the recursive Poisson solver and the usage of the parallel Schwarz method, Procedure 1 summarizes the steps to efficiently solve the discretized Poisson equation on the TLMR mesh.

3. Results and discussion

This section assesses the accuracy and efficiency of the present TLMR method and demonstrates its application to bio-inspired flow simulations, especially the simulation of groups of fish swimming together. Firstly, a convergence study is performed using two prototypical flow problems to verify its spatial and temporal discretization accuracy. Secondly, two

---

Procedure 1 Procedures to solve Poisson equation on the TLMR mesh.

1. Initialize the Pressure by a guessed ϕ^0.
2. Compute the divergence rate $\nabla \cdot \boldsymbol{u}^*$ by Eqn. (5) on each block with values in the refined regions synchronized from fine blocks by Eqn. (9).
3. Enforce boundary conditions around the computational domain.
4. Continue following iterations.
   (a) For each refined block, synchronize values ghost cell layer from the coarse parental block. If an intra-layer connection exists, replace values of the ghost cell layer of the connected region from the connected block.
   (b) Enforce boundary conditions around the immersed solid via an IBM method.
   (c) For each refinement block, solve the Poisson equation on the Cartesian grids using a multigrid method and accelerate the computation with multithreading if needed.
   (d) Check the convergence of Eqn. (5): if yes, exit iteration; otherwise, return to step 4a.

---

canonical flow problems with stationary or moving boundaries are simulated and compared to the references. Finally, flow with highly complex, non-canonical geometries is simulated to show the capabilities of the solver for complex bio-inspired flow. The computations were performed on a supercomputer that has up to 575 nodes with over 20476 cores. For the performance evaluation, nodes used for computation contain dual Intel Xeon E5-2680v3 twelve-core processors with a CPU frequency of 2.5 GHz.

3.1. Convergence study of the numerical solver on the TLMR mesh

3.1.1. The Taylor-Green vortex problem

To demonstrate the spatial and temporal discretization accuracy of our algorithm on block refinement mesh, the Taylor Green vortex flow [74], which is an unsteady flow with decaying or growing vorticity on a periodic domain, is first considered. It usually starts with an initial condition

$$
\begin{aligned}
u &= A \cos ax \sin by \sin cz, \\
v &= B \sin ax \cos by \sin cz, \\
w &= C \sin ax \sin by \cos cz,
\end{aligned}
\tag{11}
$$

where $Aa + Bb + Cc = 0$ because of the continuity equation. Exact solutions exist on a 2D domain. Within a $2\pi \times 2\pi$ periodic domain, the solution can be written as

$$
\begin{aligned}
u &= \cos x \sin y F(t), \\
v &= -\sin x \cos y F(t), \\
p &= -\frac{\rho}{4}(\cos 2x + \cos 2y) F^2(t),
\end{aligned}
\tag{12}
$$

where $A = -B = a = b = 1$ and $F(t) = e^{-2\nu t}$ is a decaying function. ν is the kinematic viscosity of the fluid and is related to the Reynolds number by $\nu = UL/Re$, where U and L are the reference velocity and length. For simplicity, the Reynolds number for the investigation is chosen as 50.
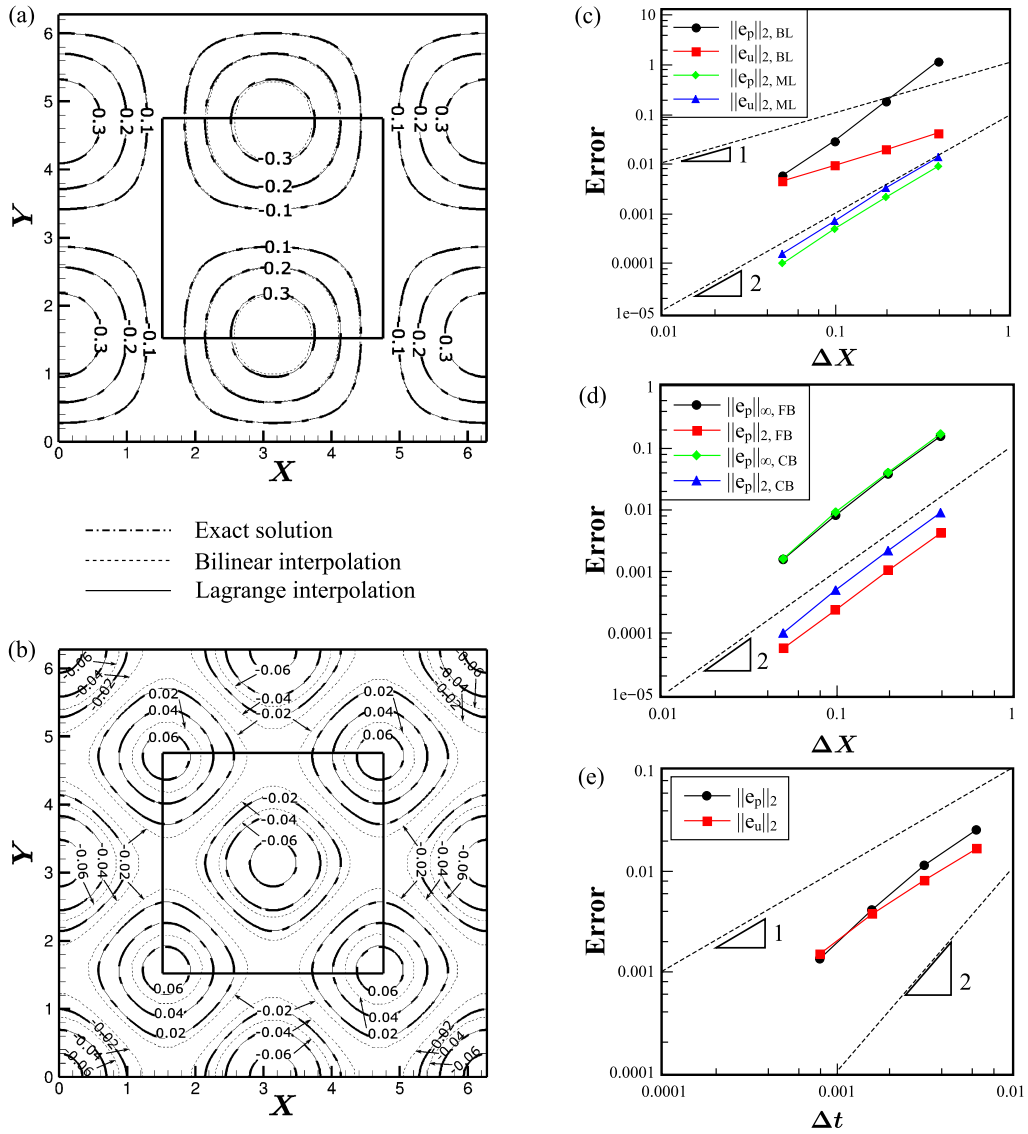
The multi-dimensional Lagrange interpolation is first examined for its role in spatial accuracy. The periodic $2\pi \times 2\pi$ domain and a $\pi \times \pi$ refined region at the center of the domain are both discretized by a 32×32 mesh and the Taylor-Green flow problem is solved on the two overlapped mesh layers using the developed solver. Fig. 6(a) and Fig. 6(b) show the contour plots of streamwise velocity (u) and pressure (p). Both the velocity and pressure match the exact solution well if the inter-layer communication employs the multi-dimensional Lagrange interpolation, as shown in Fig. 3. A simpler bilinear interpolation is adopted for comparison and yields a much bigger error in pressure, as shown in Fig. 6(b). Even worse, the error $\|\boldsymbol{e}_u\|_{2,BL}$ shows that the velocity is only first-order accurate in space with the bilinear interpolation. The normalized global error for velocity is defined by

$$
\|\boldsymbol{e_u}\|_2 = \frac{\|\boldsymbol{u} - \boldsymbol{u}_e\|_2}{\|\boldsymbol{u}_e\|_2} = \sqrt{\left(\frac{\int_\Omega \|\boldsymbol{u} - \boldsymbol{u}_e\|^2 dA/A}{\int_\Omega \|\boldsymbol{u}_e\|^2 dA/A} \right)},
\tag{13}
$$

and a normalized local error is defined by

$$
\|\boldsymbol{e_u}\|_\infty = \frac{\|\boldsymbol{u} - \boldsymbol{u}_e\|_\infty}{\|\boldsymbol{u}_e\|_2} = \frac{\max |\boldsymbol{u} - \boldsymbol{u}_e|}{\sqrt{\int_\Omega \|\boldsymbol{u}_e\|^2 dA/A}},
\tag{14}
$$

where $\boldsymbol{u}_e$ are the exact solution (12), Ω is the flow domain, and A is the area of the domain. Error for the pressure can be similarly defined. The errors on the different grids 32×32, 64×64, 128×128 and 256×256 are computed, where the corresponding finest grid resolutions are $(\pi/32) \times (\pi/32)$, $(\pi/64) \times (\pi/64)$, $(\pi/128) \times (\pi/128)$ and $(\pi/256) \times (\pi/256)$,

Fig. 6. Convergence study of the TLMR-IBM flow solver using the 2D Taylor-Green vortex flow problem: (a) and (b) contour plot of the x-component velocity u and the pressure p using bilinear interpolation or multi-dimensional Lagrange interpolation for the inter-layer communication, (c) error when using the bilinear interpolation (BL) and the multi-dimensional Lagrange interpolation (ML) for the inter-layer communication, (d) grid convergence study of the pressure on both coarse block (CB) and fine block (FB), and (e) temporal convergence study for the velocity u and pressure p.

respectively. Fig. 6(c) shows that using the multi-dimensional Lagrangian interpolation for ghost cell values, the solver can reach a global second-order accuracy for both velocity and pressure. For the pressure, as shown in Fig. 6(d), a global and local second-order accuracy in space for both the find block (FB) and the coarse block (CB) is observed via the error $\|e_p\|_{2/\infty, FB/CB}$. The simulations with grid resolution of 64×64 are further repeated with different time steps of Δt, $\Delta t/2$, $\Delta t/4$, $\Delta t/8$, where $\Delta t = 0.00633$. The error in Fig. 6(e) shows that the temporal accuracy of the solver is between the first- and second-order.

3.1.2. Flow past a fixed boundary

To investigate the accuracy of the developed algorithm with solid boundaries immersed, the classic problem of flow past a fixed circular cylinder is benchmarked. The Reynolds number $Re = U_\infty D / \nu$ is chosen 100, where D is the diameter of the cylinder. For this test, the uniform Cartesian mesh are adopted on a $4D \times 4D$ computational domain, and a $2D \times 2D$ refined block at the center. For reference, the numerical results from the in-house numerical solver [19] on a high-resolution grid (2048×2048) are taken as the reference value, since the solver is well benchmarked. The flow problem is solved using the developed TLMR algorithm on a series of grid resolutions, 32×32, 64×64, 128×128, 256×256 and 512×512 for both the
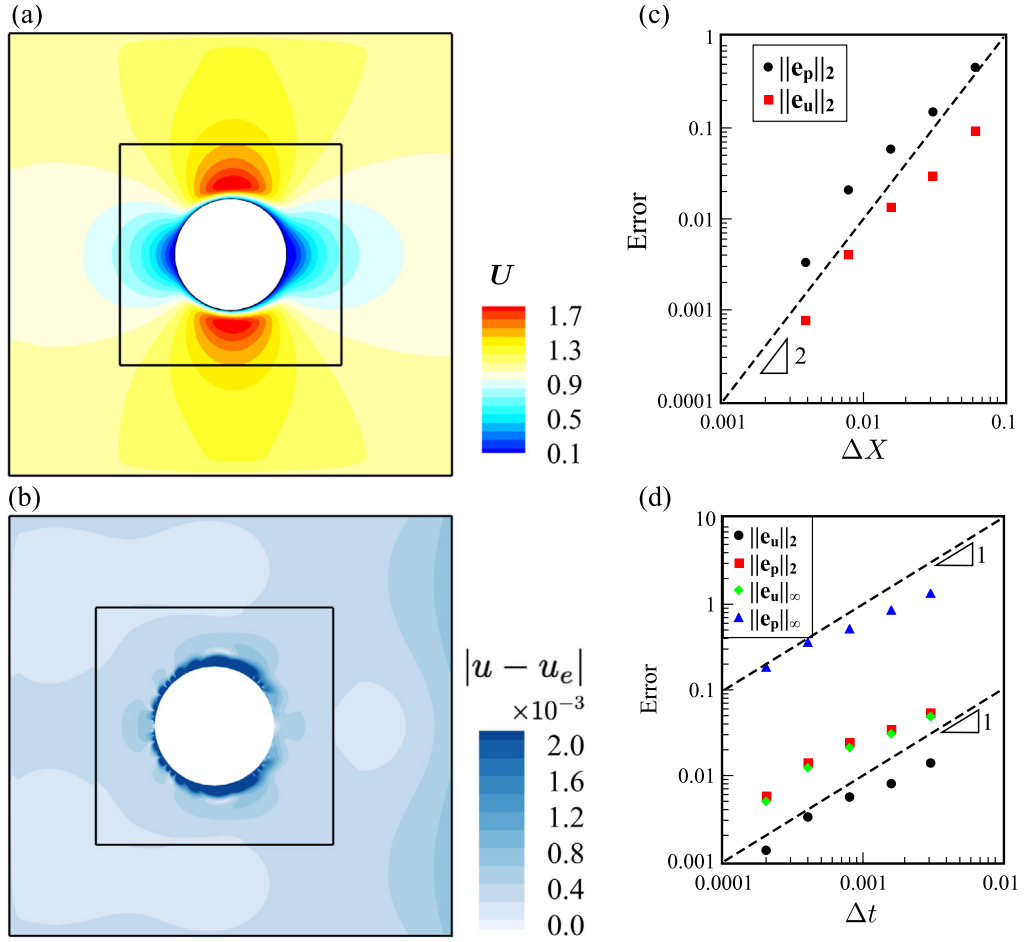
Fig. 7. Flow past stationary cylinder problem for the convergence study of the TLMR-IBM flow solver when solid boundary immersed: (a) contour plot the x-component velocity u on a 256×256 uniform mesh at $t = 0.2D/U_\infty$, (b) error of velocity $|u - u_e|$ at $t = 0.2D/U_\infty$, where u_e is the reference values computed on a uniform 2048×2048 mesh, and (c) and (d) the spatial and temporal convergence of the TLMR-IBM solver, respectively.

coarse and the fine blocks. The results are compared with the reference solution at the 2000th step, where a fixed temporal step of $0.0001D/U_\infty$ is adopted for all simulations.

Fig. 7(a) shows the streamwise velocity on a 256×256 mesh. The error of the velocity field, as shown in Fig. 7(b), indicates that the maximum error appears around the solid boundary. Mesh refinement around a solid body therefore can improve the accuracy at the boundary. The error $\|e_u\|_2$ and $\|e_p\|_2$ in Fig. 7(c) shows that velocity u and pressure p both achieve a global second-order accuracy in space. The error study in Fig. 7(d) shows that the solver is approximately first-order accurate in time for both velocity and pressure. This is consistent with Kim and Moin's conclusion [56] that the truncation error of $p = \phi$ is $O(\Delta t/Re)$.

3.2. Benchmark cases for simple flows

The following sections further benchmark the developed TLMR-IBM flow solver using two classical flows, with either stationary or moving boundaries, with results compared to the references.

3.2.1. Two-dimensional flow past a fixed circular cylinder

In many bio-inspired flow problems, the fluid is usually blocked by the body and the circulation around the body creates two rolls of vortices after the body. This phenomenon is similar to the classical problem of flow past a fixed cylinder, which is studied here to mimic the flow past the body of various swimmers. For simplicity, only 2D cases are considered with the Reynolds numbers in a range of $10^2 \sim 10^4$, as it is noticed that the Reynolds numbers for bio-inspired flow usually reside in the range of $10^2 \sim 10^6$ for insects, birds, and marine animals [75,76]. And among them, the flow is dominated by the moving boundaries and the shear layer instabilities typically when $Re < 10^5$.

Table 1
Refinement blocks for 2D cylinder simulation.

Block	Block size	Grid resolution $(\Delta = \Delta_x = \Delta_y)$	Number of mesh cells ($\times 10^6$)	Reynolds number
0	$38D \times 18D$	0.016	0.39	100, 200
1	$10D \times 4D$	0.008	0.98	-
2	$5D \times 2D$	0.004	1.64	1000, 2000, 3900
3	$3D \times 1.5D$	0.002	2.82	5000, 7000
4	$1.05D \times 1.05D$	0.001	4.15	10000

As shown in Fig. 8(a), the size of the computational domain is $38D \times 18D$, the same as the study of Singh and Mittal [77]. $D = 1$ is the diameter of the cylinder. The Dirichlet boundary condition is set at the left, top, and bottom boundaries, while the Neumann condition is applied at the outlet. The domain is discretized using the stretched Cartesian grids around a uniform region of size $12D \times 8D$ with the resolution of 0.016×0.016 around the cylinder, which is located $(10, 9)$. The Cartesian grids provide the background mesh for the refined blocks. To simulate the flow under various Reynolds numbers, up to 4 layers of refinement mesh blocks are adopted, as illustrated in Fig. 8(b). To simulate the flow under different Reynolds numbers, the number of blocks used and the corresponding resolution are listed in Table 1.

The computed drag forces on the cylinder are shown in Fig. 8(c). At low Reynolds numbers, 100 and 200, the drag forces are close to the experimental results of Wieselsberger (taken from [77]) and Tritton [78]. Since flow past a cylinder develops 3D structures at high Reynolds numbers, the 2D numerical simulation does not fit well with experimental results when the Reynolds number is higher than 200. Therefore, for a higher Reynolds number, it is reasonable to compare with other 2D numerical studies. For instance, in the range of $100 \sim 1000$, our numerical results are close to Henderson [79], who computed the unsteady flow using a spectral element method. The drag force also matches that obtained by Beaudan and Moin [80], who performed a numerical study for the 2D flow at $Re = 3900$. For higher Reynolds number ($10^3 \leq Re \leq 10^4$) our results match that of Singh and Mittal [77], who numerical studied the 2D shear layer instability using a finite element approach with deliberately fine layers of mesh surrounding the cylinder to resolve flow in the boundary layer.

The shedding period of the primary vortex (measured by the reciprocal of Strouhal number) is plotted in Fig. 8(d). At low Reynolds ($100 \sim 200$), the numerical results match the experimental data by Kovasznay and Roshko (extracted from [81]). At $Re = 3900$, the computed frequency matches those computed by Beaudan and Moin [80]. For higher Reynolds numbers, the numerically captured shedding period gently decreases with increased Re.

The instantaneous vortices after the cylinder provide visual information about the primary and shear layer instabilities. At a low Reynolds number ($100 \sim 200$), there are only two organized vortices after the cylinder. After $Re > 1000$, small shear layer instability develops but does not influence the far wake. Further increasing Re, shear layer instability becomes significant at the top and bottom of the cylinder. At $Re = 10^4$, the primary vortices are significantly reduced and the shear layer vortices start to dominate the near wake region.

Besides the aforementioned coincidence of statistical comparison with the literature, some properties in the near wake region can illustrate the value of the TLMR method in resolving flow inside the boundary layer. Fig. 9(a) shows the base suction pressure coefficient C_{pb} which is given by

$$C_{pb} = \frac{\bar{p}_{pb}}{\frac{1}{2}\rho U_\infty^2}, \tag{15}$$

where $\bar{p}_{pb}$ is the time-averaged pressure at the rear of the cylinder ($\theta = 180°$ as referenced in Fig. 10(a)). At a low Reynolds number, $Re = 100$ to be specific, the computed base pressure is coincident with the experimental results of Williamson and Roshko [82]. When $Re = 200$, a 3D flow structure yielded from secondary flow instability will cause a sudden drop of pressure [83]. Without modeling the 3D structures, our simulation only matches other 2D simulations. For instance, when $Re = 3900$, our base pressure matches that of Baudan and Moin's results. In a wide range of $Re > 2000$, our simulations are similar to that of Singh and Mittal, but with a slight difference. This might be because our finest Cartesian mesh is still relatively coarse compared to that of Singh and Mittal, who adopted a boundary layer thickness around 10^{-5} compared to 10^{-3} in the current study. The pressure distribution along the surface of the cylinder of the current solver is compared to that of Singh and Mittal to validate the refinement technique. Three different Reynolds numbers, 100, 2000, and 10000, are compared here. Our simulations show good coincidence when $\theta < 80°$, and slight discrepancies in the separation region.

Fig. 10 plots the velocity profiles of the laminar boundary layer at the Reynolds number of 10^4. The velocity is plotted in the local coordinate, where the shear velocity is tangential to the wall and varies along the wall's normal direction, as shown in the top-right corner of Fig. 10(a). The shear velocity and wall norm distance are normalized by

$$u^+ = \frac{u}{u_\tau}, \quad y^+ = \frac{y u_\tau}{\mu}, \tag{16}$$

where u_τ is the shear velocity at the wall computed by $u_\tau = \sqrt{\tau_w/\rho}$ and τ_w is the wall shear stress computed by $\tau_w = \mu \partial u/\partial y|_{y=0}$. In the current simulation, the y^+ of the cells is around 4, providing sufficient resolution for the viscous boundary layer. The flow separates from the cylinder after $\theta \geq 90°$, and therefore is not discussed here.
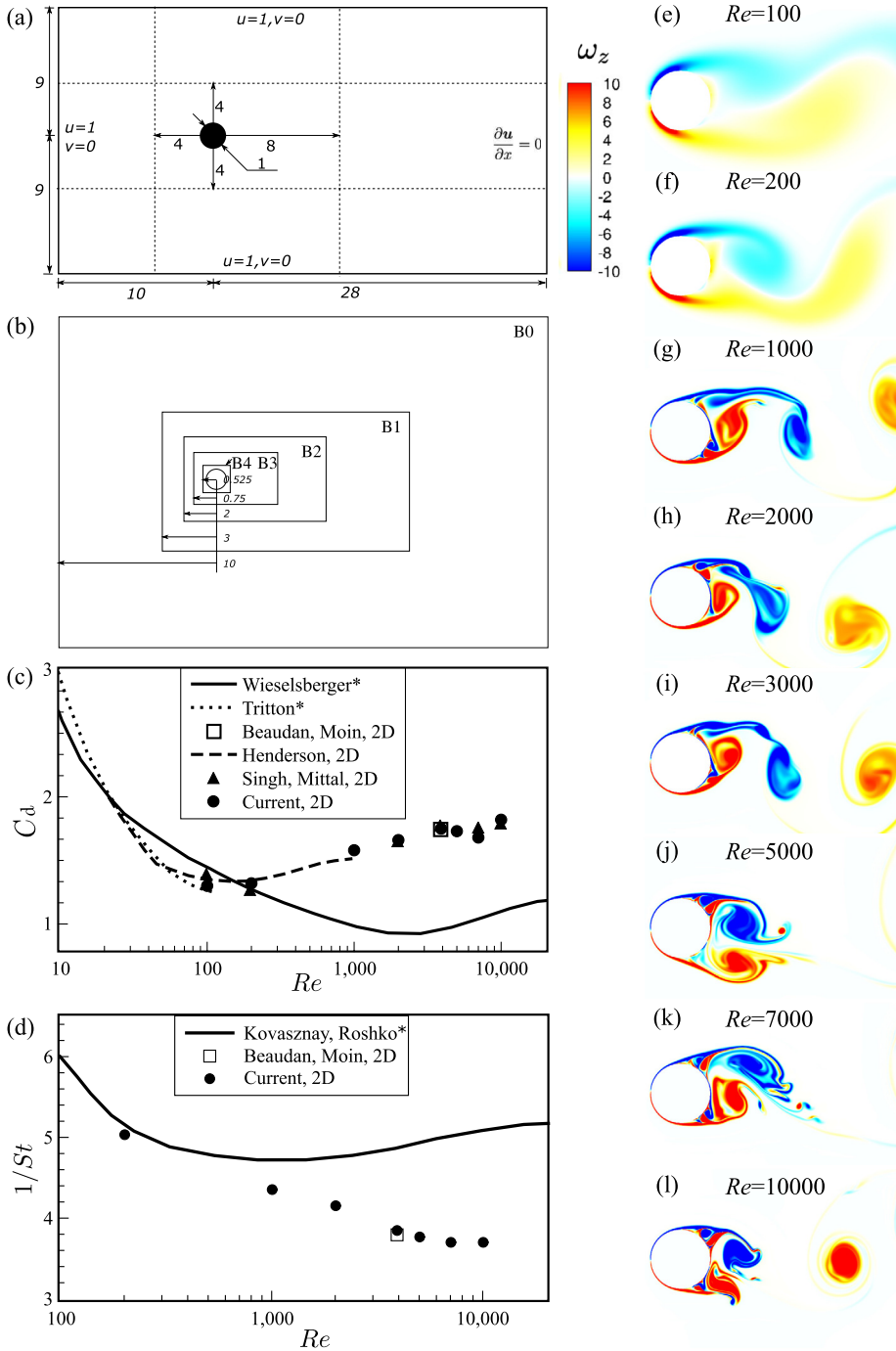
Fig. 8. A 2D simulation of flow past stationary cylinder under various Reynolds numbers: (a) set up of the 2D simulation, (b) refinement blocks configuration, (c) and (d) the drag coefficient and Strouhal number for different Reynolds numbers and (e) $\sim$ (l) the corresponding wake structures. '*' in (c) and (d) indicates experimental data with three-dimensional effects.

In the laminar boundary layer that attaches to the cylinder surface, the velocity profile along the wall-normal direction at different locations of θ is plotted in Fig. 10(a). The laminar velocity profile deviates from curve $u^+ = y^+$, which is valid for the viscous sublayer in a turbulent boundary layer. The boundary profiles derived by Hsu (see appendix F in Ref. [84]), who solved the boundary-layer equations using the wall condition and the potential flow profile as the outer boundary condition for the compressible flow, are included for comparison. Both approaches yield similar results when the distance in the y-direction is small ($y^+ < 10$). Since the potential flow has a larger velocity than the real viscous flow, the deviation becomes large when both θ and y become large.
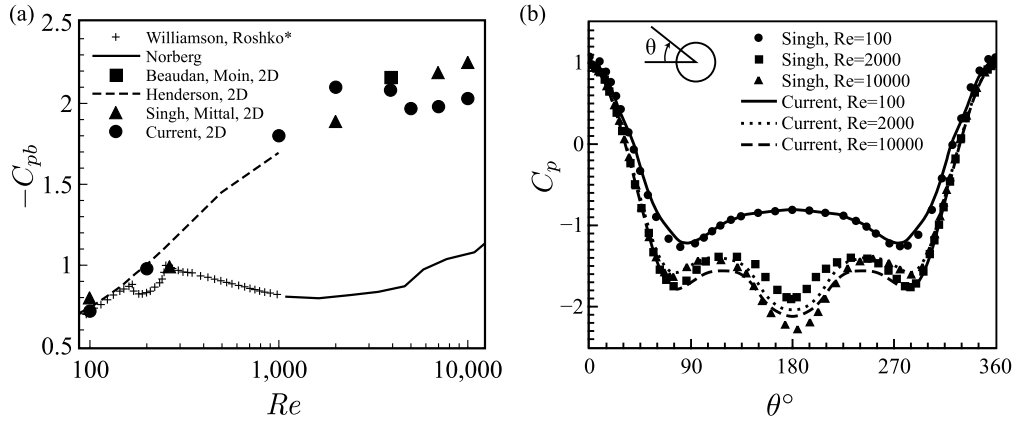
Fig. 9. Benchmark of 2D flow past a stationary cylinder: (a) base suction pressure coefficient $-C_{pb}$ and (b) averaged pressure distribution over the cylinder. '*' in (a) indicates experimental data with three-dimensional effects.
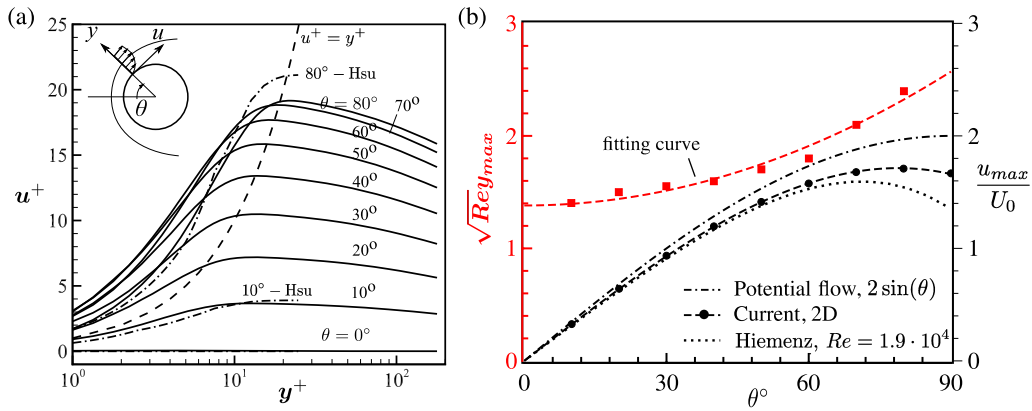

Fig. 10. The velocity profile in the shear layer of a 2D cylinder at $Re = 10^4$: (a) the shear velocity profile and (b) the maximum velocity u_{max} and thickness y_{max} at different location of θ.

On the other hand, along the wall-tangential direction, due to the curvature of the cylinder, the shear velocity can be higher than the income flow and often reaches a maximum velocity u_{max} at a height of y_{max}. For the inviscid flow, the development of u_{max} with respect to different θ is given by a simple sinusoidal relation

$$u(\theta) = U_0 \sin(\theta), \tag{17}$$

where U_0 is the incoming flow velocity. In the real flow, the velocity is retarded by the viscosity and can not reach such a high value. As the boundary layer develops along with the circular cylinder, as shown in Fig. 10(a), the thickness y_{max} and the maximum velocity u_{max} increase and the curve $u^+ = y^+$ approximately intercepts the maximum velocity from the velocity profiles at different angles of θ. The thickness y_{max} and maximum velocity u_{max} are further plotted in Fig. 10(b). When the boundary layer attaches to the surface of the cylinder, second or third-order polynomials fit well the data. Applying the boundary condition that the thickness y_{max} is symmetric and u_{max} antisymmetric at $\theta = 0$, the data are fitted by the lines

$$\sqrt{Re}\, y_{max} = 1.47 \times 10^{-4} \theta^2 + 1.38,$$
$$u_{max} = -1.77 \times 10^{-6} \theta^3 + 0.0326\theta, \tag{18}$$

where the lines are plotted aside the data points using dashed lines. From the fitted curves, the thinnest thickness is around 0.0138, and the maximum velocity in the boundary layer is around 1.7 and is below the potential flow. Our numerical results reflect this trend well. Furthermore, our numerical results are also close to the experimental results of Hiemenz at a Reynolds number of 1.9×10^4 (extracted from Ref. [85], Chapter 8.3.3). In the region of favorable pressure gradient ($\theta < 70°$), the fitted curves of u/U_0 for numerical and experimental data are close despite slightly different Reynolds numbers. In the adverse pressure gradient region, the experiments of Hiemenz clearly show that the potential velocity is difficult to recover at a higher Reynolds number. Our numerical simulation at $Re = 10^4$ experiences less velocity loss compared to that of Hiemenz, as shown in Fig. 10(b).

Table 2
Summary of the non-dimensional geometry parameters in the simulation.

Chord length, c	Span, b	Thickness, δ	Sweep angle	Aspect ratio, AR
1.0	2.51	0.016	45°	4.17
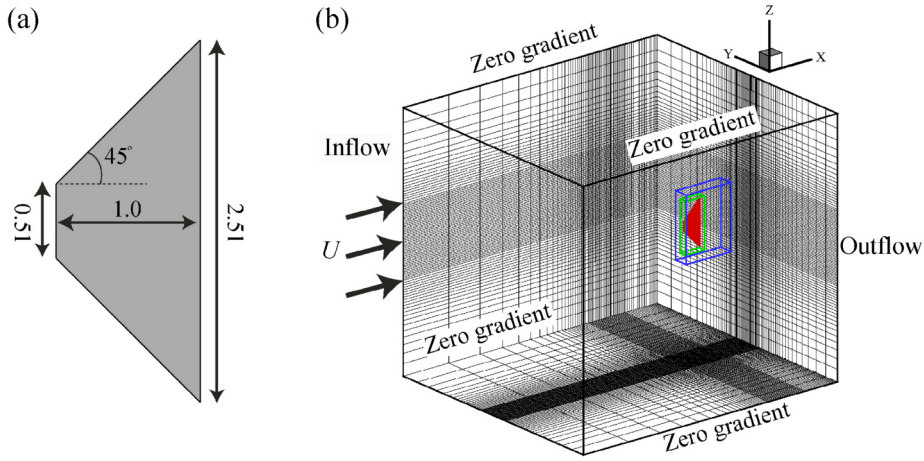
Fig. 11. Schematic of panel simulation: (a) panel geometry and (b) setup of the 3D simulation.

Table 3
Summary of refinement blocks for a 3D pitching panel simulation.

| Block	Block size	Grid resolution $(\Delta = \Delta_x = \Delta_y = \Delta_z)$	Number of mesh cells ($\times 10^6$)
0	$16.0 \times 14.0 \times 14.0$	0.0208	5.68
1	$2.8 \times 0.8 \times 3.6$	0.0104	4.13
2	$1.18 \times 0.4 \times 2.8$	0.0052	5.63

3.2.2. Three-dimensional flow past a pitching panel

Another important bio-inspired flow is the flow stirred by a thin revolving panel, like a fish fin or an insect wing. Inspired by this, a model problem with a revolving trapezoidal panel is studied. For a fair comparison, the panel geometry and kinematics are the same as the experiments of King et al. [86].

The geometry of the panel is shown in Fig. 11(a), and the associated parameters are listed in Table 2. c is the cord length of the panel and is chosen as the reference length. All dimensions are scaled respectively. The panel pitches around the leading edge following a sine wave at a frequency of $f = 1\,Hz$ and a peak-to-peak amplitude of 15°. The Strouhal number, St, and Reynolds number, Re, are defined as $St = fA/U$ and $Re = Uc/\nu$, respectively, where A denotes the peak-to-peak trailing edge amplitude, U is the incoming flow velocity, and ν indicates the kinematic viscosity of the fluid. Three Strouhal numbers, 0.27, 0.37, and 0.46, from the experiments, are chosen for the verification of the TLMR-IBM solver. According to the experiments, the variation of the Strouhal number is accomplished by changing the incoming flow velocity, and the corresponding Reynolds numbers are $Re = 10200$, 7400, and 5800, respectively.

The configuration for the numerical simulation, including the block refinement mesh and the boundary conditions are displayed in Fig. 11(b). The domain size is $16.0 \times 14.0 \times 14.0$ with total grid nodes around 5.68 million ($176 \times 144 \times 224$). To resolve the flow structures at a high Reynolds number, two layers of refined mesh blocks are employed, so the resolution is 0.0052 around the thin plate. The total number of mesh cells is around 15.4 million. In contrast, the grid number can easily go up to 1 billion ($15.4M \times 8 \times 8$) without the TLMR method. The details of the refinement blocks are summarized in Table 3. A constant inflow velocity boundary condition is assigned at the left-hand boundary, and an outflow boundary is imposed at the right-hand boundary. The zero-gradient boundary condition is set at all other lateral boundaries. For the pressure condition, the Neumann boundary is applied at all boundaries.

Fig. 12 presents the vortex wake structures under three Strouhal numbers at two different time instances, $t = 0$ and $t = 0.25T$. Fig. 12(a1-f1) are the experimentally observed wakes by King et al. [86] (courtesy of King et al.) using isosurfaces of Q-criterion [87]. Fig. 12(a2-f2) shows the numerically observed wakes, which are visualized at a value of 1% of Q_{max}, and Q isosurfaces are colored by the value of the spanwise vorticity ω_z to be consistent with the experiments. The plot shows that the numerical simulation captures the main flow features of the unsteady flow observed in the experiments. For example, the spanwise vortices are shed from the trailing edge of the panel alternatively and form the reverse Kármán vortex street. The vortex street shrinks in the spanwise direction and gradually becomes disorganized as it convects downstream. At the same time, tip vortices are generated at the ends of the panel, connecting the neighboring spanwise vortices. Furthermore,
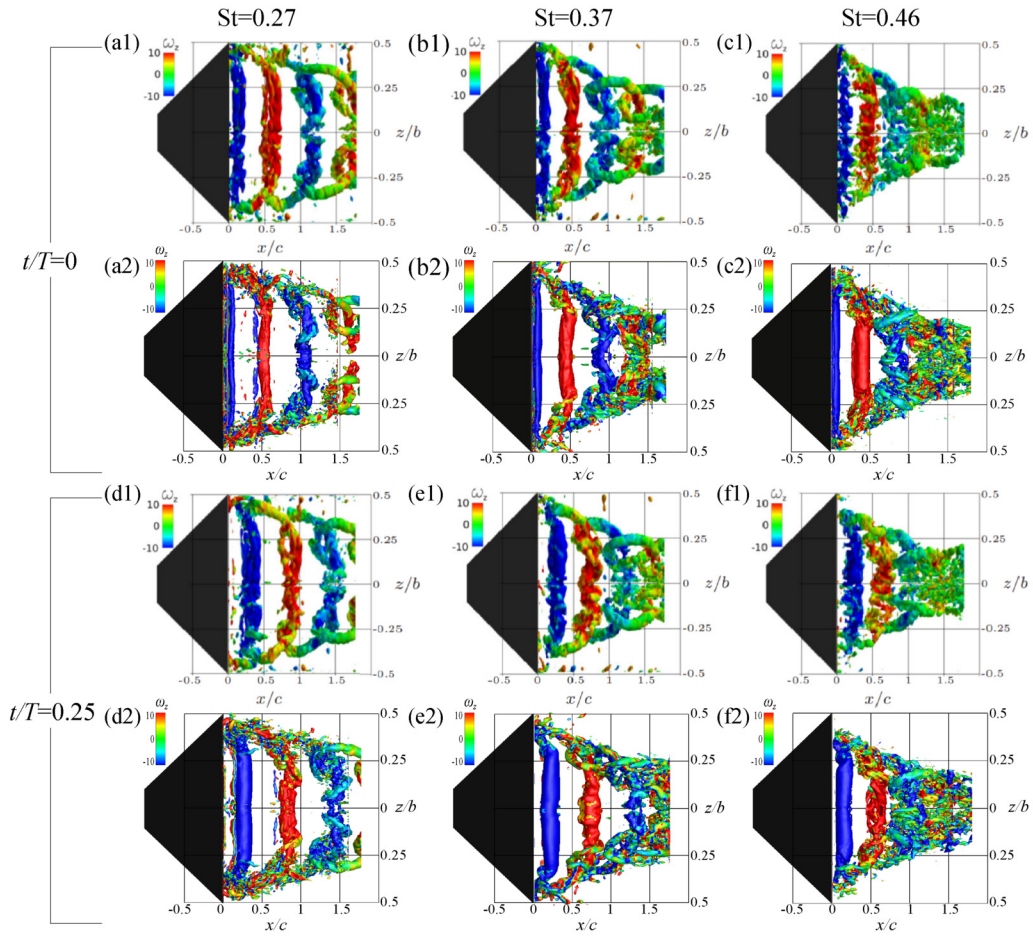
Fig. 12. Snapshots of wake structures of the pitching panel: (a1, a2, d1, d2) $St = 0.27$, (b1, b2, e1, e2) $St = 0.37$ and (c1, c2, f1, f2) $St = 0.46$ at $t = 0$ (a1-c1, a2-c2) and $t = 0.25$ (d1-f1, d2-f2) respectively. The figures (a1-f1) are from experiments results [86] (reprinted with permission from King et al.), and (a2-f2) are from current simulations.
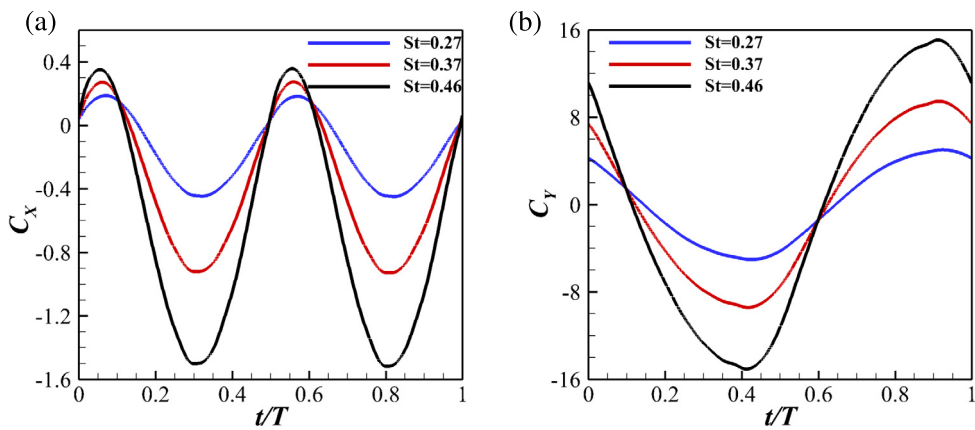
Fig. 13. Time history of force coefficients for the pitching panel: (a) coefficient of thrust C_T and (b) coefficient of lateral force C_Y.

the numerical simulations correctly reveal the dominant role of St in the development of wake structures. With increased St, the wakes are compressed heavier in the spanwise direction and the onset of wake breakdown moves upstream. For instance, at $St = 0.27$, the Q isosurface exhibits between $z/b \approx \pm 0.45$ at $x/c \approx 0.5$, and the wake breaks at $x/c \approx 1.75$ near the midspan plane (Fig. 12(a2)); while at a higher St of 0.46, the Q isosurface extents from $z/b \approx \pm 0.375$ at $x/c \approx 0.5$. In addition, the vortex tube at $x/c \approx 0.75$ become twisted and weak, and the wake breakdown begins at $x/c \approx 1.2$, where
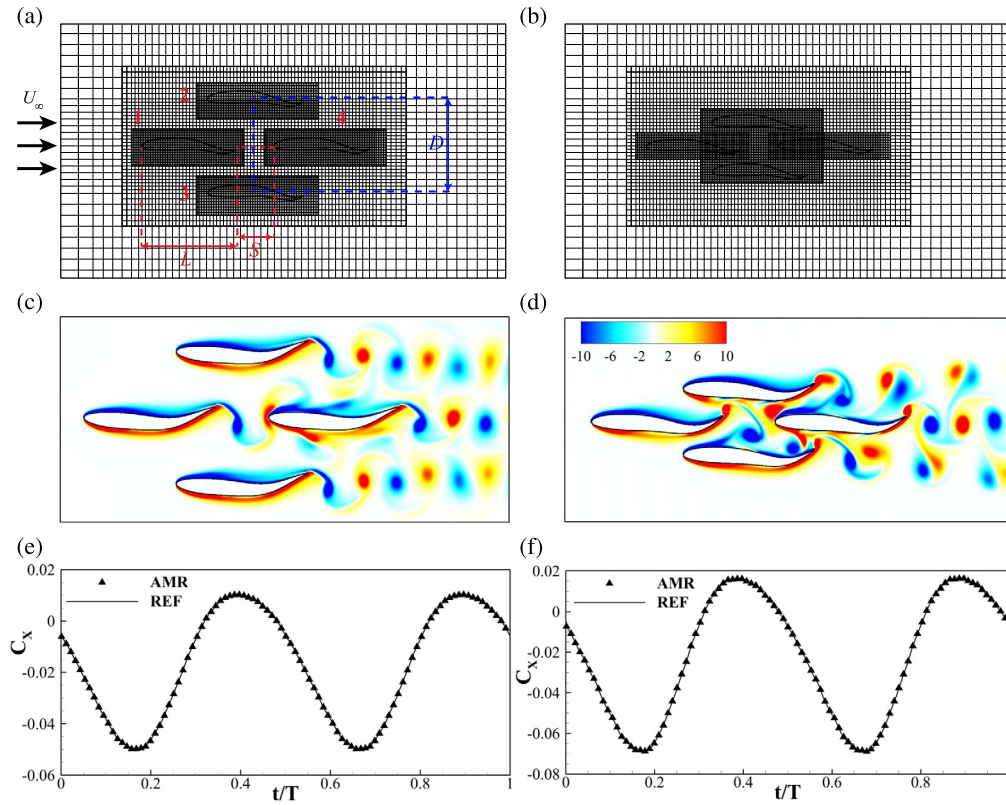
Fig. 14. Numerical study of sparse and dense schools: (a) and (b) schematic of a coarse (CASE I) and a dense (CASE II) diamond-shaped fish school with definitions of quantities describing its spatial arrangement in (a), mesh are coarsened in each direction by 4 times for easier illustration, (c) the 3S vortex streets in the sparse diamond school, (d) two 2P and one 2S vortex streets in the narrow diamond school, and (e, f) the streamwise force C_x of fish 1 in one undulating motion cycle for the sparse and dense schools respectively.

the ω_z is around zero near the midspan plane, as shown in Fig. 12(c2). The well-captured wake structures prove that the block-based mesh refinement technique could provide sufficient resolution to three-dimensional high Reynolds number problems. In addition, the time variation of the force coefficients for the three pitching panels is presented in Fig. 13 for future reference. The force coefficients are defined as $C_T = -F_X/(0.5\rho U^2 S)$ and $C_Y = F_Y/(0.5\rho U^2 S)$, where S is the area of the panel. For all cases, two peaks characterize the thrust force (C_T) in one cycle, while the lateral force (C_Y) oscillates with one peak per stroke.

3.3. The versatility and efficiency of the TLMR-IBM solver for bio-inspired flow simulations

This section demonstrates how the TLMR-IBM solver performs when multiple objects are immersed in the flow, like the flow around and within schools of fish. Both 2D and 3D cases with moving boundaries will be presented in the following studies.

3.3.1. Simulation of the two-dimensional fish school swimming problems

When fishes swim in a school, strong nonlinear body-body interactions can improve their thrust and propulsive efficiency as revealed in a recent numerical study by Pan and Dong [88]. Such a school swimming case is an excellent test case to demonstrate the efficiency of the present TLMR method.

Fig. 14(a) shows a diamond-shaped fish school formation, where L is the body length and U_∞ is the swimming speed. The S is the streamwise distance between the leading fish 1 and the trailing fish 4. The lateral spacing D is the spacing between the centers of fish 2 and fish 3. The Reynolds number for the simulation is 1000 based on the incoming flow velocity and body length. The undulating motion of fish is usually modeled by a traveling wave equation [88]. Two typical diamond-shaped schools, sparse (CASE I) and dense (CASE II), are illustrated in Fig. 14(a) and Fig. 14(b). In the sparse school, the lateral distance D is $1L$, and $0.5L$ is in the dense school. The streamwise spacing S is kept constant $0.4L$. The computation domain is of size $30L \times 20L$. With a two-layer mesh refinement, the resolution around the fishes is 0.0022×0.0022. For easier illustration, a window of $4.5L \times 3L$ around the school is plotted and the mesh is coarsened by 4 times in each direction.

Table 4

Runtime information of the 2D fish school swimming, averaged over 100 time steps.

	CASE I	CASE II	CASE III (Global Refinement)
Total mesh cells ($\times 10^6$)	1.0	1.2	6.3
Iterations of momentum	10	10	12
Iterations of Poisson	20	39	16
Time of synchronization (sec.)	0.01	0.02	-
Time of momentum solver (sec.)	0.89	0.95	10.80[a]
Time of Poisson solver (sec.)	2.84	5.20	29.16[a]
Total time of solving eqns. (sec.)	3.74	6.17	39.96[a]
Mesh speedup, $SoM(n)$	6.3	5.3	1
Speedup, $S(n)$	10.7	6.5	1
Parallel efficiency, $\eta(n)$	0.28	0.20	1

[a] Time of simulating the sparse school problem.

The simulations produce similar vortex patterns as the reference [88]. In the sparse school, a 2S vortex street is shed from each row of fishes, as shown by Fig. 14(c). In the dense school, as shown in Fig. 14(d), the top and bottom rows of fishes shed the 2P vortex streets while the middle row sheds 2S vortex streets. The streamwise force C_X of fish 1 in the school is plotted in Fig. 14(e) and 14(f). For comparison, the same school swimming problems are simulated in a single block of Cartesian grids, which are obtained by subdividing the base block in Fig. 14(a) in each direction by a factor of 4. As shown by the plots, the forces computed using the present mesh refinement technique are identical to the reference cases, which are denoted as CASE III.

Computational efficiency of the 2D fish school problems

To compare computational efficiency, Table 4 lists the runtime information of the above two simulations and a simulation of the dense school on a single Cartesian mesh as CASE III for reference. All three simulations have the same resolution of 0.0022 around the solid boundaries. The TLMR reduces the number of mesh cells of the 2D examples dramatically from 6.3 million (CASE III) to $1.0 \sim 1.2$ million (CASE I and CASE II). The reduction in the number of mesh cells significantly reduces the time in solving the discretized equations. The iterative solver for the momentum equation on the refinement mesh is $11 \sim 12$ times faster than the reference one. The speedup of the iterative Poisson solver can be 10 times, or 6 times if there are blocks intralayer-connected. This is because the iterations often increase when the intra-layer connection appears, from an average of 20 steps to 39 in current examples.

To better describe the computation efficiency, the speedup of computation is defined as the ratio of time computed on a referenced globally refined mesh (T_{GLBR}) to that on the TLMR mesh (T_{TLMR})

$$S(n) = \frac{T_{GLBR}}{T_{TLMR}} \tag{19}$$

on the n TLMR blocks. Meanwhile, as the nominal computational cost is approximately proportional to the total number of mesh cells in ideal conditions (without overhead), the nominal speedup of computation due to the savings in mesh cells ($SoM(n)$) is defined as

$$SoM(n) = \frac{N_{GLBR}}{N_{TLMR}}, \tag{20}$$

where N_{GLBR} is the number of cells of the globally refined mesh, and N_{TLMR} is the number of cells of the TLMR mesh. Conversely, the saving of mesh, or memory, can be computed from the SoM by $1 - 1/SoM(n)$. The parallel computation efficiency, $\eta(n)$, of the present mesh refinement technique computed on a distributed memory system is then assessed by

$$\eta(n) = \frac{S(n)}{SoM(n) \cdot n}. \tag{21}$$

The speedup of current examples with two layers refinement can reach as high as 10.7, in which SoM contributes 6.3. The parallel computation efficiency with three blocks, or three processors, reaches 0.28. Meanwhile, the saving in computational memory, or the number of mesh cells, can reach 84% for the 2D examples. For CASE I and CASE II, the speedup is mainly contributed by the saving of mesh by a percentage of $60\% \sim 80\%$. Noting that the values of $S(n)$ and $SoM(n)$ can vary in a certain degree for the same problem depending on different user-specific refinement strategies, such as choosing different mesh block sizes for the same object. For future reference, the relative sizes of the present TLMR blocks to the swimming objects in their maximum ranges of locomotion, namely the ratio of length ($R_L = L_{block}/L_{object}$), width ($R_W = W_{block}/W_{object}$), and height ($R_H = H_{block}/H_{object}$), are R_L=1.3 and R_W=2.0 for all 2D fish school cases and R_L=1.1, R_W=2.0, and R_H=1.3 for the 3D fish school case.

As intra-layer communication efficiency can affect the iteration time, the two communication strategies proposed in § 3 are compared. CASE II is repeated using the proposed one-interface and two-interface strategy (the default approach in
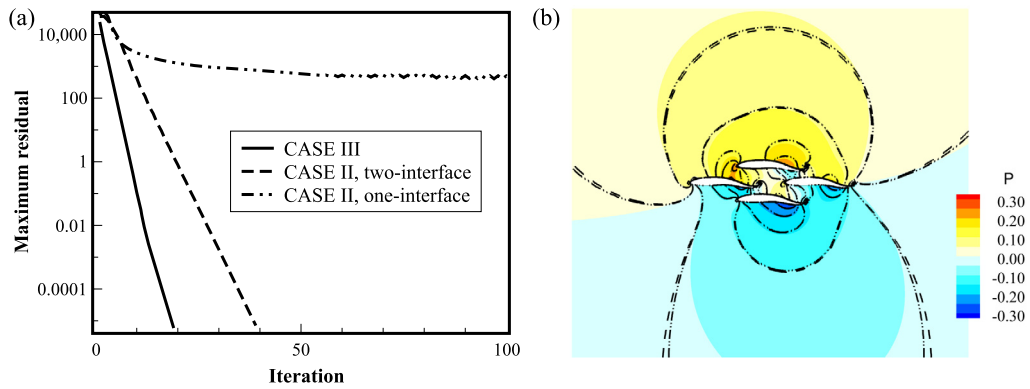
Fig. 15. Comparison of the iterative Poisson solver using two communication strategies: (a) the residual during the iterations and (b) the contour plot of the pressure. In figure (b), dash lines are for CASE II using the two-interface communication strategy, and dash-double-dot lines are for CASE II using the one-interface communication strategy, and color contour plots the results on the global refinement mesh for reference.
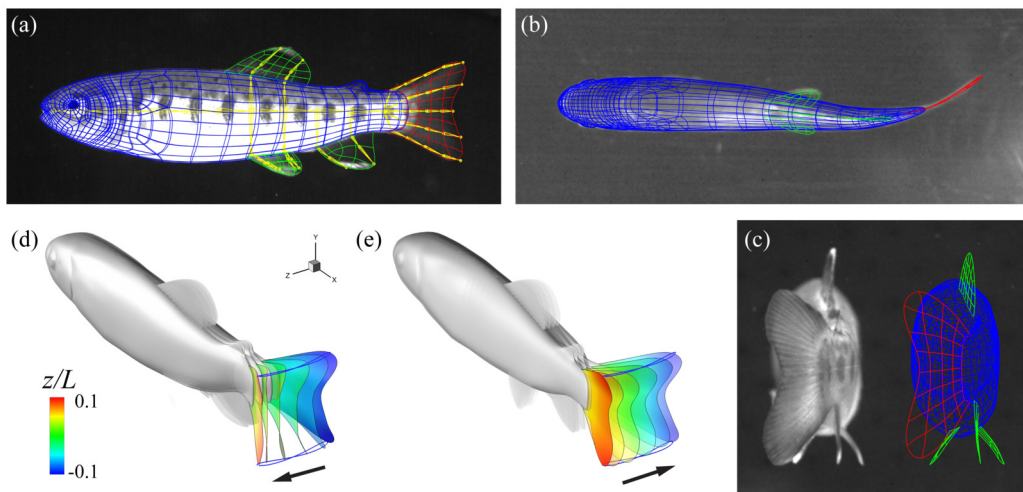
Fig. 16. Morphological and kinematical modeling of juvenile rainbow trout (*Oncorhynchus mykiss*) during steady swimming. (a-b) High-speed camera images of live rainbow trout swimming overlapped with computational model from lateral and ventral views, (c) Side-by-side comparison of live trout and computational mode from posterior view (d-e) Reconstructed swimming kinematics of computational model during left-to-right (L-to-R) and right-to-left (R-to-L) strokes, respectively.

earlier simulations) for intra-layer communication and plot the results in Fig. 15, which also includes the single block case (CASE III) for reference. Fig. 15(a) shows the maximum residual during the iteration. The multigrid algorithm is most efficient on a single Cartesian mesh, CASE III, and the Poisson equation converges in about 20 steps. The two-interface strategy of updating the outer ghost cells and iteratively solving the whole rectangular block slightly increases the iterative steps. However, the one-interface strategy needs much more steps and even thousands to converge, neutralizing the efficiency of the multigrid algorithm. Meanwhile, the two strategies yield almost identical pressure as shown in Fig. 15(b). The pressure distributions are also similar to the CASE III on a single block except for the far-field area, which is not sufficiently resolved in the current simulation due to a lack of interest there.

3.3.2. Simulation of the three-dimensional single trout swimming

The speedup of the TLMR method can be more prominent in a 3D simulation. To demonstrate the efficiency for a 3D flow with moving boundaries, the simulation of a rainbow trout (*Oncorhynchus mykiss*) is performed and compared. The trout geometry and kinematics are constructed from videos taken from an orthotropic high-speed camera system constituting a lateral, ventral, and posterior view, using the same reconstruction method adopted by Liu et al. [89,90]. The image snapshots and the reconstruction are illustrated in Fig. 16. The Reynolds number in this numerical investigation is 4800, and the Strouhal number is about 0.46.

The configuration for the simulation is shown in Fig. 17(a), and the local refinement mesh is shown in Fig. 17(b). The domain size is $10L \times 6L \times 6L$, where L is the body length of a trout. A block cutting through the body and encompassing all the fins is added as a third layer for better resolution of the flow around the undulating fins. The finest resolution is
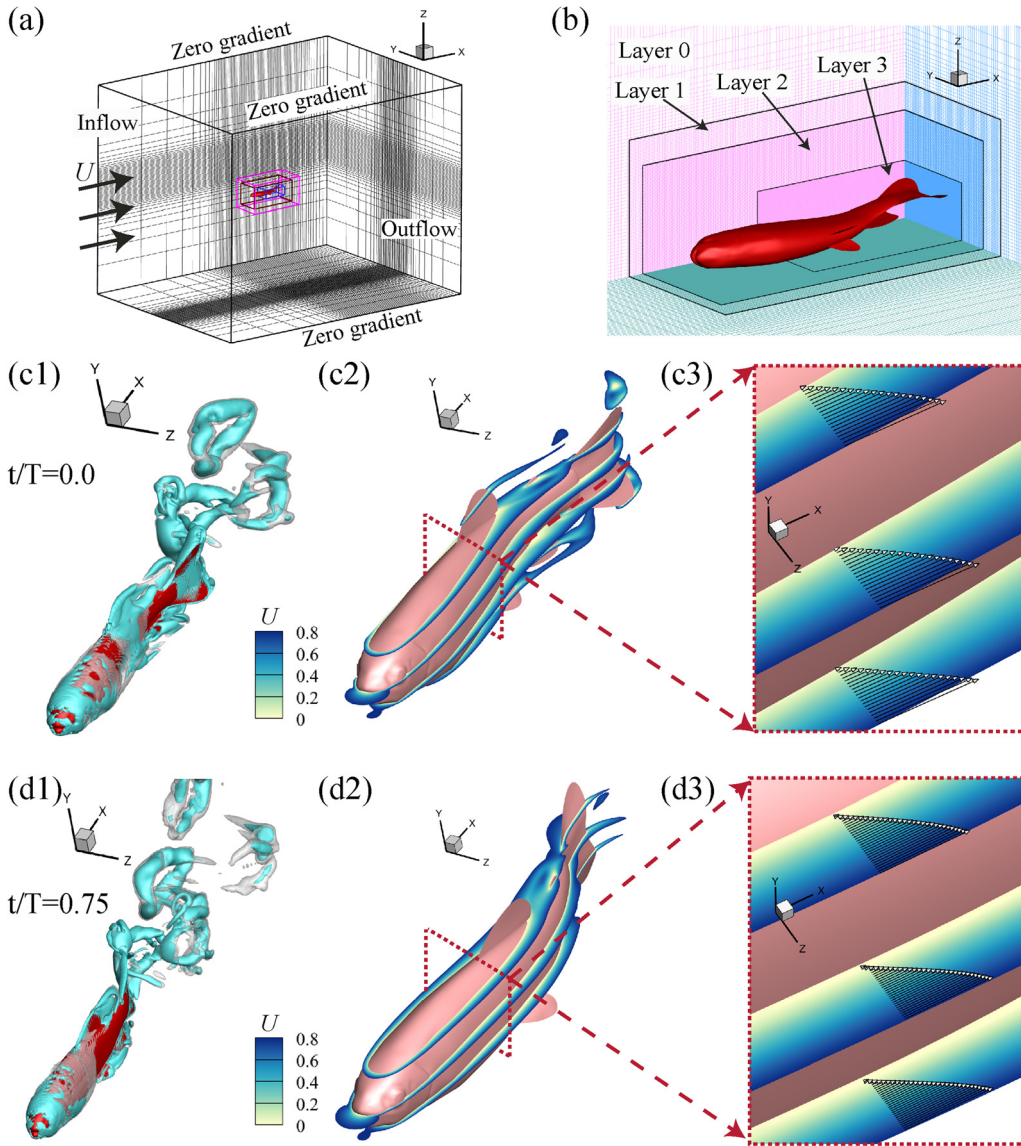
Fig. 17. Simulation of trout swimming: (a) setup of the 3D simulation, (b) local mesh refinement around solid boundary, (c1-c3) and (d1-d3) wake after trout, velocity contour on 2D slices, and velocity profile near the boundary when $t = 0T$ or $3/4T$ respectively, where T is the flapping period.

$1.75 \times 10^{-3}L$ around the posterior part of the trout. The boundary conditions are set the same as in the pitching panel cases.

The wake topology in one swimming cycle is plotted in Fig. 17(c) and Fig. 17(d). Among them, Fig. 17(c1) and (c2) show that strong coherent vortex structures are generated on the leading edge of the fins including the dorsal fin, pelvic fin, anal fin, and caudal fin. These leading-edge vortexes contribute to the majority of thrust production. Besides, in each half period of the tail-beat cycle, a vortex ring is shed from the trailing edge of the caudal fin and connects with neighboring vortex rings. The TLMR method recursively refines mesh cells around the trout. Therefore, smooth flow velocity is observed from the contour plot in the cut slices around the trout body, as shown in Fig. 17(c2) and (d2). Particularly, we plotted the boundary velocity profile in Fig. 17(c3) and (d3).

Computational efficiency of the trout swimming

To further demonstrate the efficiency of the TLMR method, the runtime information of four cases is listed and compared in Table 5. CASE I computes on a single Cartesian grid without mesh refinement. The grid resolution is 0.007 and the total number of mesh cells is about 32.8 million. Case II achieves the same resolution using the one-layer refinement, and the corresponding number of mesh cells is 7.8 million. CASE III further refines the mesh by placing one additional refinement block on top of CASE II, so the grid resolution reaches 0.0035 and the number of mesh cells is 10.4 million. CASE IV,

Table 5

Runtime information of the 3D trout simulation, averaged over 100 time steps.

	CASE I Unrefined	CASE II One layer	CASE III Two layers	CASE IV Three layers
Grid resolution ($\Delta = \Delta_x = \Delta_y = \Delta_z$)	0.007	0.007	0.0035	0.00175
Total mesh cells ($\times 10^6$)	32.8	7.8	11.6	21.5
Total cores used	4	8	12	20
Iterations of momentum	9	8	10	16
Iterations of Poisson	24	15	22	42
Time of synchronization (sec.)	-	0.30	0.63	1.32
Time of momentum solver (sec.)	34.31	4.53	9.91	20.61
Time of Poisson solver (sec.)	379.39	19.15	41.39	127.63
Total time of solving eqns. (sec.)	413.70	23.98	51.93	149.52
Mesh speedup, $SoM(n)$	1	4.2	22.6	97.7
Speedup, $S(n)$	1	17.3	63.8	177.1
Parallel efficiency, $\eta(n)$	1	2.06	0.94	0.45
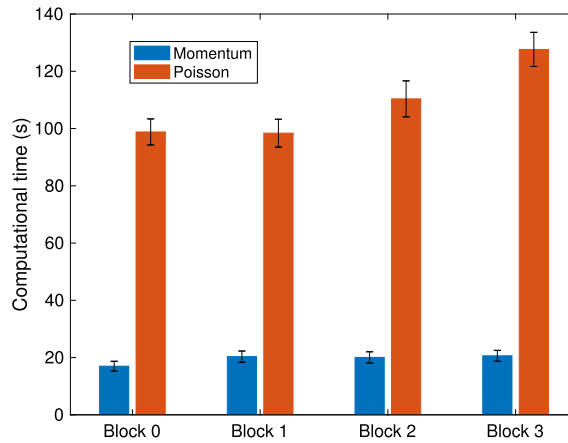
**Fig. 18.** The averaged computational time of trout simulation.

which is illustrated in Fig. 17(b), further refines CASE III to achieve a resolution of 0.00175 around the undulating tail and caudal fin. The total number of mesh cells is 21.5 million. The 3D cases are computed using four OpenMP threads for each refinement block, except that the fourth block in CASE IV uses eight threads.

To compare the computational efficiency, CASE I computed on a single Cartesian grid is chosen as the reference. The speedup $S(n)$ of one layer refinement can reach 17.3, whereas mesh-saving speedup, $SoM(n)$, is around 4.2. The speedup increases significantly when more layers of refinement are applied. For instance, it reaches 63.8 and 177.1 when applied with two and three-layer mesh refinement, respectively, whereas the mesh-saving speedup reaches up to 97.7, accounting for 55% of the total speedup. At the same time, the saving of computational memory for the 3D problem is greater than 76% and reaches a remarkable 99% when three-layer mesh refinement is applied. In the above computation, the reference cases for CASE III and CASE IV are derived from CASE I, whereas the mesh is assumed to be refined from that of CASE I in each direction by a factor of 2 or 4 respectively, and the computation time is assumed to scale linearly with the total number of mesh cells.

Fig. 18 further shows the computational time of each block in CASE IV. The number of mesh cells of the four TLMR blocks is 4.1M, 3.7M, 3.8M, and 9.9M, and the number of cores for the corresponding block is 4, 4, 4, and 8. The above setting keeps the mesh cells per core on all TLMR blocks to be around 1 million for the purpose of load balancing. The average computational time to solve the momentum equation approximately equals on all TLMR blocks. Meanwhile, the time to solve the Poisson equation varies slightly on the blocks, as shown in Fig. 18.

3.3.3. Simulation of the three-dimensional trout school swimming

This section presents results from a simulation devised to examine the hydrodynamics of fish school swimming with a significant level of complexity. The results presented here are primarily intended to show the complexity of the flow and the ability of the solver to handle a case that includes multiple moving objects with strong interactions. The fish model and flow conditions in § 3.3.2 are adopted here to study body-body and body-wake interactions in a diamond-shaped fish school with a streamwise distance of $0.4L$ and lateral spacing of $0.6L$. The flow simulation is conducted on a $12L \times 6L \times 8L$ computational domain size. A Cartesian grid of size $320 \times 96 \times 224$ and two wrapped TLMR blocks are used around each fish which provides high-resolution grids as shown in Fig. 19(a), where the finest mesh is $3.35 \times 10^{-3}L$. In the specific case presented here, the Reynolds number based on the fish body length is 5430 and the Strouhal number is 0.41. Boundary
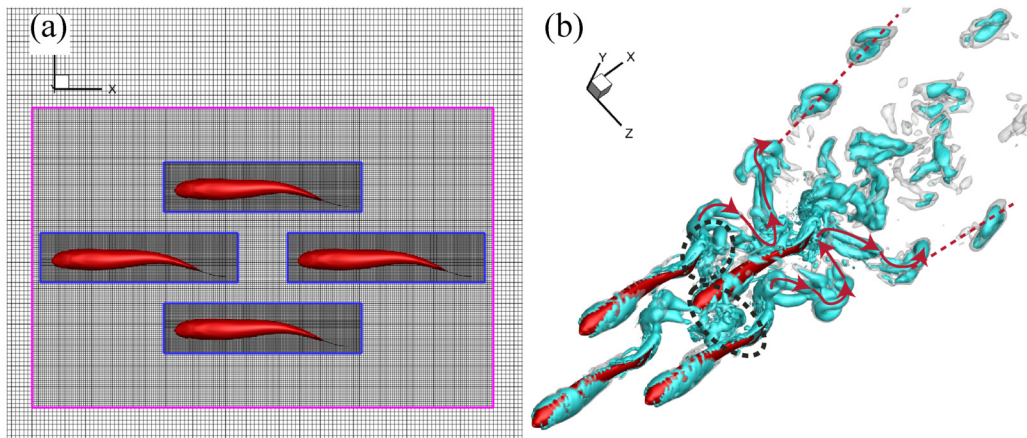
Fig. 19. (a) Top view of the computational mesh around four fishes, and (b) Q isosurfaces at the end of the 4th tail-beat of a swimming fish school.

conditions for the problem are set as shown in Fig. 17(a). The flow simulation uses 24 cores (4 cores per refinement block and a total of six blocks), 96 GB of memory, and a total of 576 CPU hours, or 24 hours of wall clock time, for computing one tail-beat cycle. Fig. 19(b) demonstrates the flow structures, which are visualized by the isosurfaces of the Q-criterion, at the end of the 4th tail-beat cycle of the fish school, where the isosurface in gray color represents $Q = 1.6$ and the one in blue color is $Q = 4.0$. At this stage, the dominant vortex features in the flow are the vortex rings and inter-connected wake vortices created during the stroke. Similar to Fig. 17, each fish sheds two sets of vortex rings downstream. Due to the existence of neighboring fishes, these vortex rings interact with the neighboring fish bodies and merge with other vortices, as shown in the circled regions in Fig. 19(b). Furthermore, due to its special position in the fish school, fish 4 interacts with the vortices shed from fish 1 as well as the half-stroke rings shed from fish 2 and fish 3, respectively. These vortices merge with the vortices produced by the tail of fish 4, then form the strong inter-connected wake vortices. This school formation is being further refined with changing of distance and tail-beat phase differences between all pairs of fish within the school and will then be used for a detailed investigation of fish school hydrodynamics.

4. Conclusions

In this paper, we have developed an efficient IB method using the TLMR for the problems of bio-inspired flows induced by the motion of single or multiple objects that use a Cartesian grid finite difference scheme for the incompressible Navier-Stokes equations. This mesh refinement approach recursively refines regions of interest by subdividing the blocks of Cartesian grids and hence enables hybrid parallelism on a distributed memory system connected by multiple computing nodes with multi-core processors. A key contribution of this paper is that it introduces a new iterative approach to solve the discretized equations on the refinement mesh for faster convergence while preserving numerical accuracy. That is, the momentum equation is discretized on all grids but the refined ones and solved using an iterative algorithm. Meanwhile, the Poisson equation is discretized on all grids and solved recursively from the coarsest block of mesh to the finest ones, of which the boundary values are interpolated and synchronized from the former. Additionally, the discretized equations are solved parallelly using the Schwarz method when the refinement blocks are connected.

Several two- and three-dimensional canonical flows are simulated and the computed results are compared with available data sets to establish the accuracy and fidelity of the new TLMR-IBM flow solver. Numerical examples without or with immersed solid boundaries, such as the Taylor-Green vortex flow and the flow past a circular cylinder, demonstrate that the new solver achieves second-order spatial accuracy for both the velocity and pressure. Simulations are also conducted for flows with a stationary or moving object at different Reynolds numbers ranging from $O(10^2)$ up to $O(10^4)$, and we show that the current solver accurately predicts the drag forces, shedding frequencies, surface pressure and boundary velocity for the canonical flow past stationary cylinder problem and the evolution of the vorticity field that matched well with the 3D PIV data of flows past a pitching plate. The computation of 2D fish school flows shows a good versatility of the TLMR method by wrapping finer mesh layers around multiple objects and a great deal of saving of the computational memory and time up to 80% by the usage of TLMR method. Finally, we demonstrate the ability of the solver to handle extremely complicated three-dimensional moving objects by showing selected results from the body- / fin-fin interactions in trout swimming and a diamond-shaped trout school swimming. These cases show that our solver not only obtains the time-resolved flow field near the fish body and in the far wakes but also permits the use of a much smaller number of mesh cells that are over 80% less than a global refinement. Consequently, the current solver saves significant computational time for the 3D problem in addition to the parallel computation, and the saving can be larger when more wrapping boxes of refinement mesh instead of a global refinement are used.

CRediT authorship contribution statement

Wei Zhang: Conceptualization, Formal analysis, Methodology, Software, Validation, Writing – original draft. **Yu Pan:** Formal analysis, Investigation, Visualization, Writing – review & editing. **Junshi Wang:** Formal analysis, Investigation, Visualization, Writing – review & editing. **Valentina Di Santo:** Data curation, Writing – review & editing. **George V. Lauder:** Data curation, Resources, Writing – review & editing. **Haibo Dong:** Conceptualization, Funding acquisition, Project administration, Resources, Supervision, Writing – review & editing.

Declaration of competing interest

The authors declare that they have no known competing financial interests or personal relationships that could have appeared to influence the work reported in this paper.

Data availability

Data will be made available on request.

Acknowledgements

References

[1] C.S. Peskin, The immersed boundary method, Acta Numer. 11 (2002) 479–517.
[2] J. Wang, Y. Ren, C. Li, H. Dong, Computational investigation of wing-body interaction and its lift enhancement effect in hummingbird forward flight, Bioinspir. Biomim. 14 (4) (2019) 046010.
[3] Z. Wu, J. Liu, J. Yu, H. Fang, Development of a novel robotic dolphin and its application to water quality monitoring, IEEE/ASME Trans. Mechatron. 22 (5) (2017) 2130–2140.
[4] J. Wang, D.K. Wainwright, R.E. Lindengren, G.V. Lauder, H. Dong, Tuna locomotion: a computational hydrodynamic analysis of finlet function, J. R. Soc. Interface 17 (165) (2020) 20190590.
[5] H. Jasak, Z. Tukovic, Automatic mesh motion for the unstructured finite volume method, Trans. FAMENA 30 (2) (2006) 1–20.
[6] T.C. Rendall, C.B. Allen, Efficient mesh motion using radial basis functions with data reduction algorithms, J. Comput. Phys. 228 (17) (2009) 6231–6249.
[7] M. Souli, A. Ouahsine, L. Lewin, ALE formulation for fluid–structure interaction problems, Comput. Methods Appl. Mech. Eng. 190 (5–7) (2000) 659–675.
[8] C.S. Peskin, Flow patterns around heart valves: a numerical method, J. Comput. Phys. 10 (2) (1972) 252–271.
[9] M.-C. Lai, C.S. Peskin, An immersed boundary method with formal second-order accuracy and reduced numerical viscosity, J. Comput. Phys. 160 (2) (2000) 705–719.
[10] R. Mittal, G. Iaccarino, Immersed boundary methods, Annu. Rev. Fluid Mech. 37 (2005) 239–261.
[11] T. Ye, R. Mittal, H. Udaykumar, W. Shyy, An accurate Cartesian grid method for viscous incompressible flows with complex immersed boundaries, J. Comput. Phys. 156 (2) (1999) 209–240.
[12] D.M. Ingram, D.M. Causon, C.G. Mingham, Developments in Cartesian cut cell methods, Math. Comput. Simul. 61 (3–6) (2003) 561–572.
[13] J. Yang, F. Stern, Sharp interface immersed-boundary/level-set method for wave–body interactions, J. Comput. Phys. 228 (17) (2009) 6590–6616.
[14] Z. Alan Wei, Z. Charlie Zheng, X. Yang, Computation of flow through a three-dimensional periodic array of porous structures by a parallel immersed-boundary method, J. Fluids Eng. 136 (4) (2014).
[15] N.J. Nair, A. Goza, A strongly coupled immersed boundary method for fluid-structure interaction that mimics the efficiency of stationary body methods, J. Comput. Phys. 454 (2022) 110897.
[16] J.D. Eldredge, A method of immersed layers on Cartesian grids, with application to incompressible flows, J. Comput. Phys. 448 (2022) 110716.
[17] J. Mohd-Yusof, Combined immersed-boundary/B-spline methods for simulations of flow in complex geometries, Center Turbul. Res. Ann. Res. Briefs 161 (1) (1997) 317–327.
[18] Y.-H. Tseng, J.H. Ferziger, A ghost-cell immersed boundary method for flow in complex geometry, J. Comput. Phys. 192 (2) (2003) 593–623.
[19] R. Mittal, H. Dong, M. Bozkurttas, F. Najjar, A. Vargas, A. Von Loebbecke, A versatile sharp interface immersed boundary method for incompressible flows with complex boundaries, J. Comput. Phys. 227 (10) (2008) 4825–4852.
[20] P. Han, G.V. Lauder, H. Dong, Hydrodynamics of median-fin interactions in fish-like locomotion: effects of fin shape and movement, Phys. Fluids 32 (1) (2020) 011902.
[21] I. Kossaczkỳ, A recursive approach to local mesh refinement in two and three dimensions, J. Comput. Appl. Math. 55 (3) (1994) 275–288.
[22] M.J. Berger, P. Colella, et al., Local adaptive mesh refinement for shock hydrodynamics, J. Comput. Phys. 82 (1) (1989) 64–84.
[23] J. Zhu, O. Zienkiewicz, Adaptive techniques in the finite element method, Commun. Appl. Numer. Methods 4 (2) (1988) 197–204.
[24] P. Solin, K. Segeth, I. Dolezel, Higher-Order Finite Element Methods, CRC Press, 2003.
[25] S. Popinet, A quadtree-adaptive multigrid solver for the Serre–Green–Naghdi equations, J. Comput. Phys. 302 (2015) 336–358.
[26] S. Popinet, Gerris: a tree-based adaptive solver for the incompressible Euler equations in complex geometries, J. Comput. Phys. 190 (2) (2003) 572–600.
[27] C. Min, F. Gibou, A second order accurate projection method for the incompressible Navier-Stokes equations on non-graded adaptive grids, J. Comput. Phys. 219 (2) (2006) 912–929.
[28] C. Burstedde, L.C. Wilcox, O. Ghattas, p4est: scalable algorithms for parallel adaptive mesh refinement on forests of octrees, SIAM J. Sci. Comput. 33 (3) (2011) 1103–1133.
[29] F. Gibou, R. Fedkiw, S. Osher, A review of level-set methods and some recent applications, J. Comput. Phys. 353 (2018) 82–109.
[30] M.J. Berger, J. Oliger, Adaptive mesh refinement for hyperbolic partial differential equations, J. Comput. Phys. 53 (3) (1984) 484–512.
[31] J. Bell, M. Berger, J. Saltzman, M. Welcome, Three-dimensional adaptive mesh refinement for hyperbolic conservation laws, SIAM J. Sci. Comput. 15 (1) (1994) 127–138.
[32] M.J. Berger, R.J. LeVeque, Adaptive mesh refinement using wave-propagation algorithms for hyperbolic systems, SIAM J. Numer. Anal. 35 (6) (1998) 2298–2316.

[33] E. Steinthorsson, D. Modiano, W. Crutchfield, J. Bell, P. Colella, An adaptive semi-implicit scheme for simulations of unsteady viscous compressible flows, in: 12th Computational Fluid Dynamics Conference, 1995, p. 1727.

[34] D. Graves, P. Colella, D. Modiano, J. Johnson, B. Sjogreen, X. Gao, A Cartesian grid embedded boundary method for the compressible Navier–Stokes equations, Commun. Appl. Math. Comput. Sci. 8 (1) (2013) 99–122.

[35] P. MacNeice, K.M. Olson, C. Mobarry, R. De Fainchtein, C. Packer, PARAMESH: a parallel adaptive mesh refinement community toolkit, Comput. Phys. Commun. 126 (3) (2000) 330–354.

[36] W. Zhang, A. Almgren, V. Beckner, J. Bell, J. Blaschke, C. Chan, M. Day, B. Friesen, K. Gott, D. Graves, et al., AMReX: a framework for block-structured adaptive mesh refinement, J. Open Sour. Softw. 4 (37) (2019) 1370, https://doi.org/10.21105/joss.01370.

[37] P. Colella, D.T. Graves, T. Ligocki, D. Martin, D. Modiano, D. Serafini, B. Van Straalen, Chombo software package for AMR applications - design document, Available at the Chombo website: http://seesar.lbl.gov/ANAG/chombo/(September2008), 2009.

[38] A.M. Wissink, R.D. Hornung, S.R. Kohn, S.S. Smith, N. Elliott, Large scale parallel structured AMR calculations using the SAMRAI framework, in: Proceedings of the 2001 ACM/IEEE Conference on Supercomputing, 2001, p. 6.

[39] A. Dubey, A. Almgren, J. Bell, M. Berzins, S. Brandt, G. Bryan, P. Colella, D. Graves, M. Lijewski, F. Löffler, et al., A survey of high level frameworks in block-structured adaptive mesh refinement packages, J. Parallel Distrib. Comput. 74 (12) (2014) 3217–3227.

[40] L.H. Howell, J.B. Bell, An adaptive mesh projection method for viscous incompressible flow, SIAM J. Sci. Comput. 18 (4) (1997) 996–1013.

[41] A.S. Almgren, J.B. Bell, P. Colella, L.H. Howell, M.L. Welcome, A conservative adaptive projection method for the variable density incompressible Navier–Stokes equations, J. Comput. Phys. 142 (1) (1998) 1–46.

[42] M. Vanella, P. Rabenold, E. Balaras, A direct-forcing embedded-boundary method with adaptive mesh refinement for fluid–structure interaction problems, J. Comput. Phys. 229 (18) (2010) 6427–6449.

[43] C. Liu, C. Hu, Block-based adaptive mesh refinement for fluid–structure interactions in incompressible flows, Comput. Phys. Commun. 232 (2018) 104–123.

[44] J. Yang, An easily implemented, block-based fast marching method with superior sequential and parallel performance, SIAM J. Sci. Comput. 41 (5) (2019) C446–C478.

[45] B.E. Griffith, R.D. Hornung, D.M. McQueen, C.S. Peskin, An adaptive, formally second order accurate version of the immersed boundary method, J. Comput. Phys. 223 (1) (2007) 10–49.

[46] IBAMR: an adaptive and distributed-memory parallel implementation of the immersed boundary method, https://ibamr.github.io/.

[47] J. Green, P. Jimack, A. Mullis, J. Rosam, Towards a three-dimensional parallel, adaptive, multilevel solver for the solution of nonlinear, time-dependent, phase-change problems, Parallel, Distrib. Grid Comput. Eng. 21 (2009) 251–274.

[48] R.D. Hornung, J.A. Trangenstein, Adaptive mesh refinement and multilevel iteration for flow in porous media, J. Comput. Phys. 136 (2) (1997) 522–545.

[49] S. Verma, G. Novati, P. Koumoutsakos, Efficient collective swimming by harnessing vortices through deep reinforcement learning, Proc. Natl. Acad. Sci. USA 115 (23) (2018) 5849–5854.

[50] M. Daghooghi, I. Borazjani, The hydrodynamic advantages of synchronized swimming in a rectangular pattern, Bioinspir. Biomim. 10 (5) (2015) 056018.

[51] G. Li, D. Kolomenskiy, H. Liu, B. Thiria, R. Godoy-Diana, On the energetics and stability of a minimal fish school, PLoS ONE 14 (8) (2019) e0215265.

[52] J.-H. Seo, R. Mittal, Improved swimming performance in schooling fish via leading-edge vortex enhancement, Bioinspir. Biomim. 17 (6) (2022) 066020.

[53] Y.-F. Peng, R. Mittal, A. Sau, R.R. Hwang, Nested Cartesian grid method in incompressible viscous fluid flow, J. Comput. Phys. 229 (19) (2010) 7072–7101.

[54] X. Deng, H. Dong, A highly efficient sharp-interface immersed boundary method with adaptive mesh refinement for bio-inspired flow simulations, in: APS Division of Fluid Dynamics Meeting Abstracts, 2017, pp. Q30–002.

[55] W. Zhang, Y. Pan, Y. Gong, H. Dong, J. Xi, A Versatile BM-Based AMR Method for Studying Human Snoring, Fluids Engineering Division Summer Meeting, vol. 85284, American Society of Mechanical Engineers, 2021, V001T02A039.

[56] J. Kim, P. Moin, Application of a fractional-step method to incompressible Navier-Stokes equations, J. Comput. Phys. 59 (2) (1985) 308–323.

[57] D.L. Brown, R. Cortez, M.L. Minion, Accurate projection methods for the incompressible Navier–Stokes equations, J. Comput. Phys. 2 (168) (2001) 464–499.

[58] H. Dong, R. Mittal, F. Najjar, Wake topology and hydrodynamic performance of low-aspect-ratio flapping foils, J. Fluid Mech. 566 (2006) 309.

[59] H. Dong, M. Bozkurttas, R. Mittal, P. Madden, G. Lauder, Computational modelling and analysis of the hydrodynamics of a highly deformable fish pectoral fin, J. Fluid Mech. 645 (2010) 345.

[60] G. Liu, H. Dong, C. Li, Vortex dynamics and new lift enhancement mechanism of wing–body interaction in insect forward flight, J. Fluid Mech. 795 (2016) 634–651.

[61] Y. Saad, M.H. Schultz, GMRES: a generalized minimal residual algorithm for solving nonsymmetric linear systems, SIAM J. Sci. Stat. Comput. 7 (3) (1986) 856–869.

[62] H.A. Van der Vorst, Bi-CGSTAB: a fast and smoothly converging variant of bi-CG for the solution of nonsymmetric linear systems, SIAM J. Sci. Stat. Comput. 13 (2) (1992) 631–644.

[63] H.L. Stone, Iterative solution of implicit approximations of multidimensional partial differential equations, SIAM J. Numer. Anal. 5 (3) (1968) 530–558.

[64] G. Schneider, M. Zedan, A modified strongly implicit procedure for the numerical solution of field problems, Numer. Heat Transf. 4 (1) (1981) 1–19.

[65] M. Zedan, G. Schneider, A three-dimensional modified strongly implicit procedure for heat conduction, AIAA J. 21 (2) (1983) 295–303.

[66] H.A. Schwarz, Ueber einige abbildungsaufgaben, Ges. Math. Abh. 11 (1869) 65–83.

[67] P.-L. Lions, On the Schwarz alternating method. I, in: First International Symposium on Domain Decomposition Methods for Partial Differential Equations, vol. 1, Paris, France, 1988, p. 42.

[68] Y. Saad, Iterative Methods for Sparse Linear Systems, SIAM, 2003.

[69] M.J. Gander, Schwarz methods over the course of time, Electron. Trans. Numer. Anal. 31 (2008) 228–255.

[70] S.R. Fulton, P.E. Ciesielski, W.H. Schubert, Multigrid methods for elliptic problems: a review, Mon. Weather Rev. 114 (5) (1986) 943–959.

[71] J.H. Bramble, Multigrid Methods, Chapman and Hall/CRC, 2019.

[72] R. Wienands, W. Joppich, Practical Fourier Analysis for Multigrid Methods, Chapman and Hall/CRC, 2004.

[73] T. Guillet, R. Teyssier, A simple multigrid scheme for solving the Poisson equation with arbitrary domain boundaries, J. Comput. Phys. 230 (12) (2011) 4756–4771.

[74] G.I. Taylor, A.E. Green, Mechanism of the production of small eddies from large ones, Proc. R. Soc. Lond. Ser. A, Math. Phys. Sci. 158 (895) (1937) 499–521.

[75] C.P. Ellington, The aerodynamics of hovering insect flight. I. The quasi-steady analysis, Philos. Trans. R. Soc. Lond. B, Biol. Sci. 305 (1122) (1984) 1–15.

[76] G.S. Triantafyllou, M. Triantafyllou, M. Grosenbaugh, Optimal thrust development in oscillating foils with application to fish propulsion, J. Fluids Struct. 7 (2) (1993) 205–224.

[77] S. Singh, S. Mittal, Flow past a cylinder: shear layer instability and drag crisis, Int. J. Numer. Methods Fluids 47 (1) (2005) 75–98.

[78] D.J. Tritton, Experiments on the flow past a circular cylinder at low Reynolds numbers, J. Fluid Mech. 6 (4) (1959) 547–567.

[79] R.D. Henderson, Details of the drag curve near the onset of vortex shedding, Phys. Fluids 7 (9) (1995) 2102–2104.

[80] P.B. Beaudan, Numerical experiments on the flow past a circular cylinder at sub-critical Reynolds number, Ph.D. thesis, Stanford University, 1995.

[81] A. Roshko, Experiments on the flow past a circular cylinder at very high Reynolds number, J. Fluid Mech. 10 (3) (1961) 345–356.

[82] C.H.K. Williamson, Oblique and parallel modes of vortex shedding in the wake of a circular cylinder at low Reynolds numbers, J. Fluid Mech. 206 (1989) 579–627, https://doi.org/10.1017/S0022112089002429.

[83] C.H.K. Williamson, Three-dimensional wake transition, J. Fluid Mech. 328 (1996) 345–407, https://doi.org/10.1017/S0022112096008750.

[84] H.-w. Hsu, Numerical solution of laminar compressible flow over a circular cylinder, Master's thesis, Georgia Institute of Technology, 1972.

[85] H. Schlichting, K. Gersten, Boundary Layer Theory, Springer, 2015.

[86] J.T. King, R. Kumar, M.A. Green, Experimental observations of the three-dimensional wake structures and dynamics generated by a rigid, bioinspired pitching panel, Phys. Rev. Fluids 3 (3) (2018) 034701.

[87] J.C. Hunt, A.A. Wray, P. Moin, Eddies, streams, and convergence zones in turbulent flows, in: Studying Turbulence Using Numerical Simulation Databases, 2. Proceedings of the 1988 Summer Program, 1988.

[88] Y. Pan, H. Dong, Computational analysis of hydrodynamic interactions in a high-density fish school, Phys. Fluids 32 (12) (2020) 121901.

[89] G. Liu, Y. Ren, H. Dong, O. Akanyeti, J.C. Liao, G.V. Lauder, Computational analysis of vortex dynamics and performance enhancement due to body–fin and fin–fin interactions in fish-like locomotion, J. Fluid Mech. 829 (2017) 65–88.

[90] G. Liu, B. Geng, X. Zheng, Q. Xue, H. Dong, G.V. Lauder, An image-guided computational approach to inversely determine in vivo material properties and model flow-structure interactions of fish fins, J. Comput. Phys. 392 (2019) 578–593.